mathematics

MDPI

Article

Probabilistic BESS Scheduling for Duck-Curve Mitigation Under Correlated DER Penetration in Distribution Systems

Sami M. Alshareef [1,*], Ahmed Fathy [1] and Yasser O. Assolami [2]

[1] Department of Electrical Engineering, College of Engineering, Jouf University, Sakaka 72388, Saudi Arabia; afali@ju.edu.sa
[2] Department of Electrical Engineering, College of Engineering and Architecture, Umm Al-Qura University, Makkah 24382, Saudi Arabia; yoassolami@uqu.edu.sa
* Correspondence: smalshareef@ju.edu.sa

Abstract

High penetration levels of photovoltaic (PV) generation and electric vehicles (EVs) exacerbate the duck-curve effect in distribution systems. This paper proposes a probabilistic scheduling framework for battery energy storage systems (BESSs) to mitigate substation power variability under uncertain and correlated distributed energy resource (DER) penetration. Correlated PV, EV, and BESS penetration scenarios are generated by Gaussian-copula-based Monte Carlo sampling, weighted by a fuzzy duck-curve relevance index, and reduced to ten representative scenarios by K-means clustering; their substation power profiles are obtained with OpenDSS. BESSs are allocated to the six buses with the highest power variability and scheduled in 2-h intervals using a three-state (charge, idle, discharge) binary encoding. For each scenario, a day-ahead schedule is optimized with an improved binary Equilibrium Optimizer (IBiEO). On the IEEE 34-bus feeder, IBiEO achieves the lowest probability-weighted objective, 48.0% below the no-action case, and significantly outperforms four of five binary benchmark algorithms under equal evaluation budgets, while performing comparably to a hybrid DBA-PSO algorithm. The OpenDSS-validated schedules reduce the probability-weighted maximum ramp, peak-to-valley range, and evening ramp by 38.2%, 47.4%, and 53.8%, respectively. Under Monte Carlo propagation of the measurement uncertainty of the state-of-charge estimate, BESS capacity, and PV peak power, the probability-weighted mean improvement of the duck-curve indices remains 25.2% (95% coverage interval: 20.4–29.7%). These findings demonstrate the effectiveness of the proposed framework in mitigating the duck-curve effect under correlated DER penetration and device-parameter uncertainty, supporting the reliable integration of high PV and EV shares in distribution systems.

Keywords: duck-curve mitigation; battery energy storage systems; probabilistic scheduling; distributed energy resources; improved binary equilibrium optimizer; distribution systems; OpenDSS

MSC: 90C15; 90C27

Academic Editor: Anatoliy Swishchuk

Received: 25 September 2026
Revised: 26 October 2026
Accepted: 2 November 2026
Published: 4 November 2026

Copyright: © 2026 by the authors. Licensee MDPI, Basel, Switzerland. This article is an open access article distributed under the terms and conditions of the Creative Commons Attribution (CC BY) license.

1. Introduction

1.1. Background and Motivation

The increasing penetration of renewable energy sources (RESs), particularly photovoltaic (PV) generation, is reshaping the operation of modern distribution systems. Declining PV costs and the need to reduce greenhouse-gas emissions have accelerated PV deployment worldwide [1,2]. At the same time, the growing adoption of electric vehicles (EVs) introduces new and potentially flexible electricity demand. The combined presence of distributed PV generation and EV charging can substantially alter the temporal and spatial characteristics of distribution-system power flows. High PV penetration can produce the well-known duck-curve profile, which represents the net demand that remains after accounting for renewable generation [3,4]. During daylight hours, increasing PV output reduces net demand and can create a pronounced midday minimum. As PV generation declines toward sunset while demand remains relatively high, the net demand increases rapidly, resulting in a steep evening ramp. This behavior increases the need for flexible resources and can impose additional ramping and balancing requirements on the power system. EV charging can further influence the net-load profile because its magnitude and timing depend on EV penetration and charging behavior. When charging coincides with periods of high demand, it can aggravate peak loading and evening ramps; when appropriately coordinated, EV charging can instead provide demand-side flexibility. BESSs provide another important flexibility resource by shifting energy between periods of high PV availability and periods of high net demand. Consequently, coordinated management of PV generation, EV charging, and BESS operation can provide an effective means of reducing substation power variability and mitigating the duck-curve effect. However, the operating conditions of these distributed energy resources (DERs) are inherently uncertain. PV and EV penetration can vary across locations and operating periods, while their penetration levels may also exhibit statistical dependence. Therefore, a BESS schedule optimized for a single deterministic operating condition may not provide satisfactory performance across the range of conditions encountered in practical distribution systems. This motivates a probabilistic scheduling framework capable of representing the uncertainty and correlation of DER penetration while maintaining computational tractability.

1.2. Related Work and Research Gap

Various approaches have been investigated to mitigate the operational effects of high PV penetration. EV integration and coordinated charging have been studied from perspectives including charging infrastructure allocation, energy-loss reduction, generation scheduling, cost minimization, and load-profile smoothing [5–10]. Demand-side strategies, including smart load shedding and residential pre-cooling, have also been proposed to modify demand during critical periods [11,12]. Other studies have considered PV curtailment, alternative PV configurations, and advanced inverter control to reduce midday generation and associated net-load variations [13–17]. BESSs have received considerable attention because of their ability to shift energy temporally and directly address the characteristic midday-to-evening transition of the duck curve. Storage scheduling has been investigated using dynamic pricing, optimal control, pumped-hydro storage, hybrid energy-storage technologies, and metaheuristic optimization [18–24]. Residential BESSs have also been considered for increasing PV self-consumption and reducing the adverse effects of high PV penetration [25]. More integrated approaches have combined BESSs with EVs, including battery-swapping systems, to exploit available storage capacity for temporal energy shifting [26]. Recent studies have further investigated coordinated and forecast-assisted BESS dispatch for mitigating PV-induced reverse power flow, reducing

https://doi.org/10.3390/math14214040

grid exchanges, and alleviating duck-curve effects [27]. Despite these developments, many existing approaches are formulated for deterministic or limited operating conditions. PV penetration, EV adoption, and storage capacity are commonly represented by fixed values, and the BESS schedule is optimized for a specific operating condition. Such formulations may be insufficient when DER penetration varies substantially across the operating space. Probabilistic methods have been introduced to address uncertainty in DER-integrated systems. Monte Carlo simulation has been used to model stochastic EV characteristics and determine storage requirements [6], while probabilistic duck and ramp curves have been developed to represent uncertainty under high PV penetration using statistical dependence models [28]. Load-forecast uncertainty associated with distributed energy resources has also been investigated using real-world demand data [29]. These studies demonstrate the importance of probabilistic modeling; however, the joint and correlated uncertainty of PV, EV, and storage penetration has received limited attention in distribution-level BESS scheduling for duck-curve mitigation. Furthermore, directly incorporating a large number of Monte Carlo realizations into time-series distribution-system optimization can result in a substantial computational burden. Although scenario-reduction techniques can alleviate this problem, the relative importance of different operating conditions should also be considered when selecting representative scenarios. In addition, BESS placement is commonly determined using electrical, economic, or optimization-based criteria, whereas identifying locations according to temporal power variability can directly target buses associated with significant net-load fluctuations. Recent studies have demonstrated the potential of optimization-based BESS scheduling for reducing PV-induced ramps and duck-curve effects [26,28]. Nevertheless, a unified framework that captures correlated DER penetration uncertainty, assigns importance to operating scenarios, reduces the scenario set, identifies critical BESS locations from temporal variability, and determines a BESS schedule effective across representative scenarios remains limited. This gap motivates the probabilistic framework proposed in this paper. Table 1 compares representative duck-curve mitigation studies with the proposed approach.

Table 1. Comparison of duck-curve mitigation studies with the proposed approach.

Reference	Test System	DERs	Duck-Curve Mitigation	Optimization Approach	EVs	Stochastic Modeling *		PV–EV Correlation	BESS Scheduling
						PV	EV		
[6]	IEEE 33-bus	PEV, BESS	×	Nonlinear programming	✓	×	×	×	✓
[7]	California ISO	PV, EVs	✓	Quadratic programming	✓	×	×	×	✓
[8]	Residential system	PV, EVs	✓	Quadratic and linear programming	✓	×	×	×	✓
[9]	Commercial MG	PV, ESS, EVs	×	MILP	✓	×	×	×	✓
[11]	Pakistan system	PV, BESS, EVs	✓	Smart load shedding	✓	×	×	×	✓
[12]	Residential system	PV, pre-cooling	✓	Pre-cooling strategy	×	×	×	×	—
[13]	—	PV, BESS	✓	Improved Gamma-type inverter	✓	×	×	×	✓
[14]	—	Bifacial PV	✓	MIQP	×	×	×	×	—
[15]	IEEE 24-bus RTS	High–penetration PV, BESS,	✓	MILP	×	×	×	×	✓

		curtailment, load shedding							
[16]	IEEE 69-bus	Bifacial PV	✓	Analytical method	×	×	×	×	—
[18]	—	Distributed storage	✓	Bilevel programming	×	×	×	×	✓
[19]	Real system	PV, pumped-hydro storage	✓	Dynamic programming	×	×	×	×	✓
[20]	Taiwan grid	RES, hydro storage	✓	MATPOWER	×	×	×	×	✓
[21]	Real system	Battery, green hydrogen, hybrid storage	✓	Model-based framework	×	✓	×	×	✓
[23]	IEEE 33-bus	PV, BESS	✓	PSO	×	×	×	×	✓
[25]	Residential system	PV, household BESS	✓	Measurement-based analysis	×	×	×	×	✓
[26]	—	PV, BESS, battery-swapping EVs	✓	Battery swapping and energy shifting	✓	×	×	×	✓
[27]	Real system	PV, BESS	✓	LP-GA-DNN	×	×	×	×	✓
[28]	Qinghai system	PV	✓	KDE, discrete convolution, and copula	×	✓	×	×	—
[30]	—	Reused-battery ESS	✓	ESS-based approach	×	×	×	×	✓
[31]	California ISO	PV, EVs, BESS	×	MILP	✓	×	×	×	✓
[32]	Residential system	PV	✓	Evolutionary algorithm	×	×	×	×	—
[33]	Real system	PV (two 1.5 MW plants), BESS	✓	Whale optimization	×	×	×	×	✓
[34]	IEEE 1547	PV, BESS, DSTATCOM	✓	Third-order G.I. + FLL	×	×	×	×	✓
[35]	Belgian grids	Wind, solar, thermal units	✓	Multi-timescale optimization	×	✓	×	×	✓
[22]	Smart grid	Pumped hydro, CSP, thermal units	✓	PSO + hybrid PSO	×	×	×	×	✓
[36]	Real system	EV chargers, BESS	✓	Five-step optimization	✓	×	×	×	✓
[37]	Real system	Multi-pumped storage	✓	Random forest + Lagrange optimization	×	✓	×	×	✓
[38]	Alberta market	PV, BESS	✓	Merit-order and market analysis	×	×	×	×	✓
The current work	IEEE 34-bus	PV, EVs, BESS	✓	IBiEO	✓	✓	✓	✓	✓

✓: Considered, ×: Not considered; MILP: Mixed-Integer Linear Programming; MIQP: Mixed-Integer Quadratic Programming; PSO: Particle Swarm Optimization; BiEO: Binary Equilibrium Optimizer; BPSO: Binary Particle Swarm Optimizer; BDA: Binary Bat Algorithm; DBA-PSO: Detective Behavior Algorithm and PSO; Stochastic modeling*: the PV output and/or the EV penetration or charging behavior is represented by random variables or scenarios. The term does not denote a metrological measurement-uncertainty budget [39].

1.3. Work Contributions

This paper proposes an integrated probabilistic framework for mitigating the duck-curve effect through BESS scheduling under uncertain and correlated PV, EV, and BESS penetration. The main contributions are summarized as follows:

- **Correlation-aware scenario modeling:** A Monte Carlo framework incorporating prescribed correlations among PV, EV, and BESS penetration is integrated with fuzzy scenario weighting and K-means clustering to identify a compact set of representative operating conditions for probabilistic scheduling.
- **Variability-based BESS siting and three-state scheduling:** BESS locations are selected based on bus-level temporal power variability, while a two-bit encoding enables charging, idling, and discharging in 2-h intervals. Scenario-specific day-ahead schedules are optimized using OpenDSS-derived baseline profiles, with the forecast scenario determining the implemented schedule.
- **Improved binary optimization: A**n improved binary Equilibrium Optimizer (IBiEO) is developed by incorporating an elitist memory pool, greedy selection, bit-flip mapping, and stagnation-triggered restart to address the discrete BESS scheduling problem.
- **Statistically validated evaluation and robustness assessment:** On the modified IEEE 34-bus feeder, IBiEO is compared with five binary benchmark algorithms under an identical budget of 7500 fitness evaluations and 30 independent runs, and every schedule is validated by 24-h OpenDSS simulation. IBiEO attains the lowest expected objective, 48.0% below the no-action case, and improves the probability-weighted duck-curve indices by 36.1%. Robustness is further assessed with respect to forecast errors, BESS size, and the measurement uncertainty of the SOC estimate, BESS capacity, and PV peak power (JCGM 101:2008).

2. Research Methodology

2.1. Overall Framework of the Proposed Method

The proposed framework coordinates the BESSs to mitigate substation power variability under uncertain DER penetration. As illustrated in Figure 1, the methodology integrates probabilistic scenario generation, duck-curve-relevance assessment, scenario reduction, BESS location identification, and coordinated scheduling within an unbalanced distribution-system model.

A modified IEEE 34-bus radial feeder with aggregated residential load, EV charging, PV generation, and BESSs is considered. Correlated Monte Carlo sampling generates joint DER penetration scenarios, which are evaluated by a fuzzy inference system according to their duck-curve characteristics. K-means clustering is then applied to obtain representative scenarios. Candidate BESS locations are identified from the temporal variability of the feeder power profile, and the BESS schedules are optimized using the IBiEO algorithm with a probabilistic duck-curve objective. The optimized schedules are subsequently evaluated through time-series power-flow simulations in OpenDSS (Electric Power Research Institute, Palo Alto, CA, USA). The resulting framework integrates the probabilistic characterization of DER penetration levels and scenario reduction with coordinated BESS scheduling while preserving the spatial and temporal characteristics of the distribution feeder. In this paper, two sources of uncertainty are distinguished. The first is the planning-level variability of DER penetration, that is, the unknown number of EVs, PV units, and BESSs connected at the residential aggregation buses, which is represented by correlated random penetration scenarios (Section 2.4). The second is the metrological uncertainty of device parameters, such as the SOC estimate, the usable BESS capacity, and the PV peak power at standard test conditions. This measurement uncertainty is propagated

through the power-flow simulations by the Monte Carlo method of the Guide to the Expression of Uncertainty in Measurement (GUM) Supplement 1 [39], and its effect on the duck-curve indices is quantified in Section 4.7

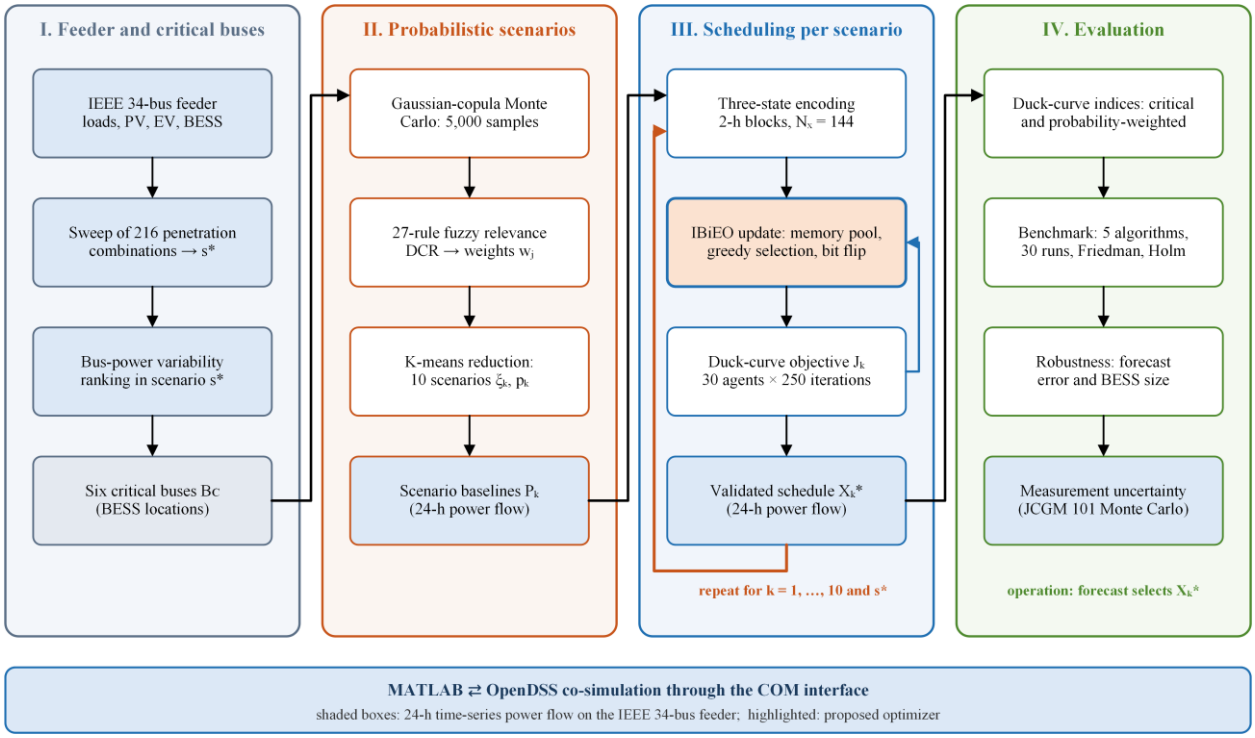


Figure 1. Proposed probabilistic BESS scheduling framework: (I) feeder modeling and critical-bus identification; (II) correlated scenario generation, fuzzy weighting, and reduction; (III) scenario-specific BESS scheduling with IBiEO; (IV) OpenDSS-based evaluation. $\boldsymbol{s}^*$ denotes the critical scenario, and $\mathbf{X}_{\boldsymbol{k}}^*$ the optimized schedule of scenario $\boldsymbol{k}$.

2.2. Distribution Feeder and DER Formulation

2.2.1. Modified IEEE 34-Bus Feeder

The proposed method is evaluated on a modified IEEE 34-bus radial distribution feeder. The original feeder topology and electrical parameters are retained, including its unbalanced three-phase configuration, phase-dependent loads, voltage-regulation equipment, shunt capacitors, and distribution transformers. The complete set of feeder buses is defined as:

$$B = \{1, 2, \ldots, 34\} \tag{1}$$

Ten residential aggregation buses are introduced at selected feeder locations. These buses form a subset of the complete feeder-bus set and are denoted by:

$$B_R = \{B_{R,1}, B_{R,2}, \ldots, B_{R,10}\} \subseteq B \tag{2}$$

The residential aggregation locations are illustrated in Figure 2. Each aggregation bus represents a group of residential customers and may have different load, EV, PV, and BESS characteristics.

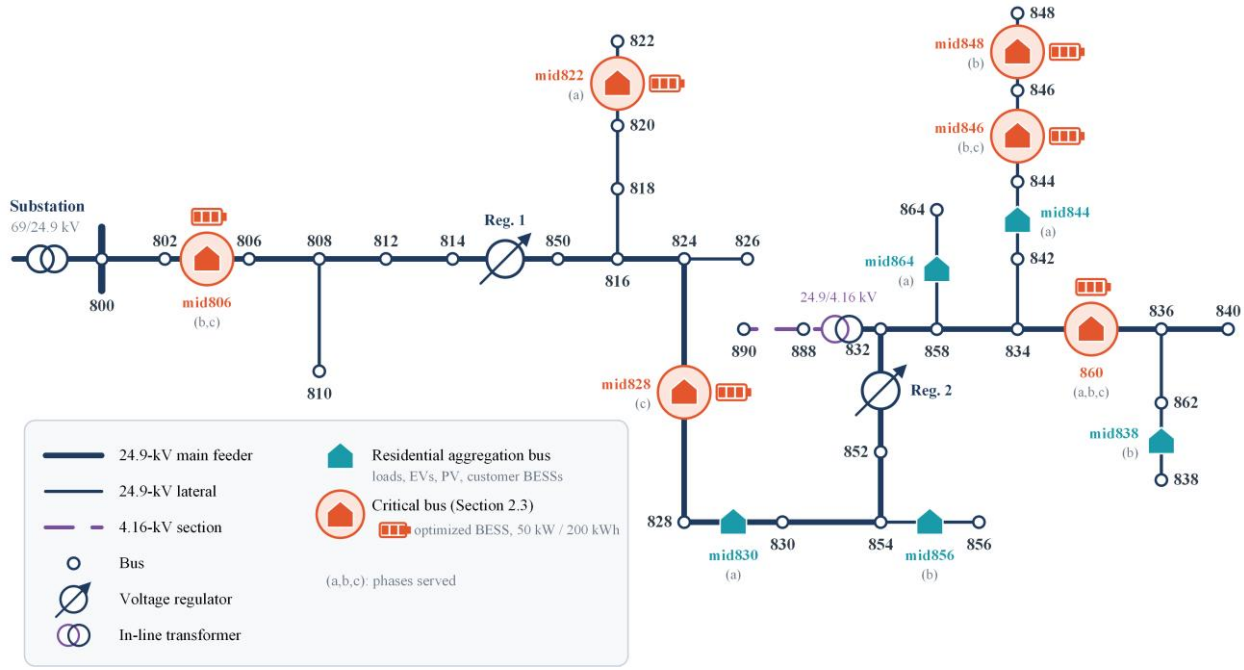


Figure 2. Modified IEEE 34-bus distribution feeder with residential aggregation buses and the six critical buses selected for BESS scheduling.

2.2.2. Residential Demand

Let $T = \{1, \ldots, N_T\}$denote the hourly simulation horizon, with $N_T = 24$. Let $\mathcal{H}_i$denote the households represented at aggregation bus i. The active-power demand of household $h \in \mathcal{H}_i$is computed as follows:

$$P^{L}_{i,h,t} = P^{L,\text{rated}}_{i,h} \lambda^{L}_{i,h,t}, i \in \mathcal{B}_R, h \in \mathcal{H}_i, t \in \mathcal{T} \tag{3}$$

where $P^{L,\text{rated}}_{i,h}$is the reference demand and $\lambda^{L}_{i,h,t}$is the normalized hourly load profile. The aggregated load at bus i can be expressed as:

$$P^{L}_{i,t} = \sum_{h \in \mathcal{H}_i} P^{L}_{i,h,t} \tag{4}$$

2.2.3. EV Charging

Let $\mathcal{E}_i$ denote the EVs associated with aggregation bus i. The charging power of EV $e \in \mathcal{E}_i$at time t is modeled as:

$$P^{EV}_{i,e,t} = P^{EV,\text{rated}}_{i,e} \lambda^{EV}_{i,e,t} \tag{5}$$

where $P^{EV,\text{rated}}_{i,e}$is the rated charging power and $\lambda^{EV}_{i,e,t} \in [0, 1]$ represents its normalized charging profile at time t. Accordingly, the aggregate EV demand at bus i is given by:

$$P^{EV}_{i,t} = \sum_{e \in \mathcal{E}_i} P^{EV}_{i,e,t} \tag{6}$$

The total EV charging demand across the feeder is then expressed as:

$$P^{EV}_{t} = \sum_{i \in \mathcal{B}_R} P^{EV}_{i,t} \tag{7}$$

2.2.4. PV Generation

Let $\mathcal{P}_i$ denote the PV units located at aggregation bus i. The generated power of PV unit $p \in \mathcal{P}_i$ is calculated as follows:

$$P_{i,p,t}^{PV} = P_{i,p}^{PV,\text{rated}} \lambda_{i,p,t}^{G} \lambda_t^{W} \tag{8}$$

where $P_{i,p}^{PV,\text{rated}}$ denotes the rated capacity of PV unit p, $\lambda_{i,p,t}^{G} \in [0,1]$ represents the normalized solar profile, and λ_t^{W} accounts for weather-dependent effects, including irradiance and temperature. Therefore, the PV output satisfies the following:

$$0 \le P_{i,p,t}^{PV} \le P_{i,p}^{PV,\text{rated}} \tag{9}$$

The aggregate PV generation at bus i and across all residential aggregation buses is expressed as:

$$P_{i,t}^{PV} = \sum_{p \in \mathcal{P}_i} P_{i,p,t}^{PV} \tag{10}$$

$$P_t^{PV} = \sum_{i \in \mathcal{B}_R} P_{i,t}^{PV} \tag{11}$$

2.2.5. BESS Model

Let $\mathcal{S}_i$ denote the BESS units associated with bus i. A signed power convention is adopted, where positive power represents discharging and negative power represents charging as follows:

$$P_{i,s,t}^{B} = P_{i,s,t}^{dis} - P_{i,s,t}^{ch} \tag{12}$$

The charging and discharging powers satisfy the following formulas:

$$0 \le P_{i,s,t}^{ch} \le P_{i,s}^{ch,\max} \tag{13}$$

$$0 \le P_{i,s,t}^{dis} \le P_{i,s}^{dis,\max} \tag{14}$$

Hence,

$$-P_{i,s}^{ch,\max} \le P_{i,s,t}^{B} \le P_{i,s}^{dis,\max} \tag{15}$$

The normalized SOC is constrained as:

$$SOC_{i,s}^{\min} \le SOC_{i,s,t} \le SOC_{i,s}^{\max} \tag{16}$$

Its temporal evolution is calculated as:

$$SOC_{i,s,t+1} = SOC_{i,s,t} + \frac{\eta_{ch} P_{i,s,t}^{ch} \Delta t}{E_{i,s}} - \frac{P_{i,s,t}^{dis} \Delta t}{\eta_{dis} E_{i,s}} \tag{17}$$

where $E_{i,s}$ is the usable energy capacity, and η_{ch} and η_{dis} are the charging and discharging efficiencies. Since the study uses hourly simulations, $\Delta t = 1$ h. Each optimized BESS has a usable capacity of 200 kWh and a rated power of 50 kW. The charging and discharging efficiencies are set to $\eta_{ch} = \eta_{dis} = 0.95$, which corresponds to the 90% round-trip efficiency of commercial residential lithium-ion systems [40]. The SOC is bounded by $[\text{SOC}_{\min}, \text{SOC}_{\max}] = [0.2,1.0]$, where the lower bound limits the depth of discharge, a dominant driver of cycle ageing in lithium-ion batteries [41]. The initial SOC is set to 0.8, and the terminal-SOC penalty (93)–(94) penalizes any deviation of the final SOC from this value, so that the daily schedule is approximately periodic and can be applied on consecutive days. The influence of uncertainty in these parameters, notably in the SOC estimate and the usable capacity, is quantified in Section 4.7.

The aggregate BESS power at bus i is as follows:

$$P_{i,t}^{B} = \sum_{s \in \mathcal{S}_i} P_{i,s,t}^{B} \tag{18}$$

With this convention, positive $P_{i,t}^{B}$ reduces feeder demand, whereas negative $P_{i,t}^{B}$ increases feeder demand.

2.2.6. Net Feeder Demand

The net active-power demand at aggregation bus i is computed as follows:

$$P_{i,t}^{net} = P_{i,t}^{L} + P_{i,t}^{EV} - P_{i,t}^{PV} - P_{i,t}^{B} \tag{19}$$

The corresponding total feeder-level net demand is defined as:

$$P_{t}^{net} = P_{t}^{L} + P_{t}^{EV} - P_{t}^{PV} - P_{t}^{B} \tag{20}$$

The substation active power obtained from the network solution is expressed as follows:

$$P_{t}^{sub} = P_{t}^{L} + P_{t}^{EV} - P_{t}^{PV} - P_{t}^{B} + P_{t}^{loss} \tag{21}$$

where P_{t}^{loss} denotes the feeder active-power losses. The resulting feeder formulation provides substation power, bus voltages, branch flows, and feeder losses. This procedure establishes a direct link between residential DER operation and the electrical response of the complete feeder.

2.3. Critical-Bus Identification

BESS control locations are selected according to the temporal variability of bus power. For each non-source bus b,

$$\Delta P_{b}(t) = |P_{b}(t) - P_{b}(t-1)|, \;\; t = 2, \ldots, N_{T} \tag{22}$$

and the corresponding variability index is expressed as:

$$V_{b} = \sum_{t=2}^{N_{T}} \Delta\, P_{b}(t) \tag{23}$$

The source bus is excluded because it represents the feeder reference. The remaining buses are ranked according to V_b, and the six buses with the largest variability indices are selected as critical buses:

$$\mathcal{B}_{C} = \{b_{1}, b_{2}, \ldots, b_{N_{C}}\}, \; N_{C} = 6 \tag{24}$$

Restricting the optimization to these locations reduces the control dimension while concentrating BESS actions at buses exhibiting the largest temporal power variations. The variability index is evaluated in the critical scenario s^{*} defined in (67), i.e., the combination of EV, PV, and customer-BESS penetration that produces the steepest substation ramp among the 216 combinations {0, 10, …, 50}[3]. Evaluating the index under this worst-case condition places the BESSs where the duck-curve variation is most severe; the resulting buses and their contribution to the substation profile are analyzed in Section 4.1.

2.4. Correlated Monte Carlo Generation of DER Scenarios

2.4.1. Correlation Modeling

The statistical dependence among EV, PV, and BESS penetration levels is represented using a Gaussian copula. For Monte Carlo realization j, where N_{MC} = 5000 is the number of Monte Carlo samples ($j = 1, \ldots, N_{MC}$),

$$z^{(j)} = \begin{bmatrix} z_{EV}^{(j)} \\ z_{PV}^{(j)} \\ z_{B}^{(j)} \end{bmatrix} \sim \mathcal{N}(0, R) \tag{25}$$

where

$$R = \begin{bmatrix} 1 & \rho_{EV,PV} & \rho_{EV,B} \\ \rho_{EV,PV} & 1 & \rho_{PV,B} \\ \rho_{EV,B} & \rho_{PV,B} & 1 \end{bmatrix} \tag{26}$$

The coefficients $\rho_{EV,PV}$, $\rho_{EV,B}$, and $\rho_{PV,B}$ define the dependence structure among the DER penetration variables. In this study, $\rho_{EV,PV}$ = 0.6, $\rho_{EV,B}$ = −0.3, and $\rho_{PV,B}$ = 0.5. These coefficients are planning assumptions rather than estimates from measured data. The positive coefficients represent the tendency of residential customers who install PV to also adopt EVs and home batteries [42,43], whereas the negative EV–BESS coefficient reflects partial substitution: a household that owns an EV already has access to a large flexible battery and is therefore less likely to install a stationary BESS. For (25) to define a valid joint distribution, R must be symmetric and positive definite; this holds for the selected values, whose smallest eigenvalue is 0.056.

2.4.2. Feeder Representation

The correlated Gaussian samples are transformed into uniform variables using the standard-normal cumulative distribution function:

$$u_q^{(j)} = \Phi\left(z_q^{(j)}\right), \quad q \in \{EV, PV, B\} \tag{27}$$

The corresponding penetration levels are as follows:

$$N_q^{(j)} = N_q^{\max} u_q^{(j)} \tag{28}$$

Hence, the j-th Monte Carlo scenario is expressed as:

$$\xi^{(j)} = \left[N_{EV}^{(j)} \quad N_{PV}^{(j)} \quad N_B^{(j)}\right]^T \tag{29}$$

The resulting samples preserve the rank dependence imposed by the Gaussian copula while mapping each variable onto its prescribed penetration range. Since $\Phi(\cdot)$ transforms each standard-normal component of z into a uniform variable on [0, 1], every penetration level is marginally uniform on [0, $N_q^{\max}$], with $N_{EV}^{\max} = N_{PV}^{\max} = N_B^{\max} = 50$. The Gaussian assumption is therefore confined to the dependence structure: the penetration levels are uniformly distributed individually, whereas their joint behavior inherits the correlations prescribed by R. Figure 3 illustrates the generated samples of z and the corresponding penetration levels.

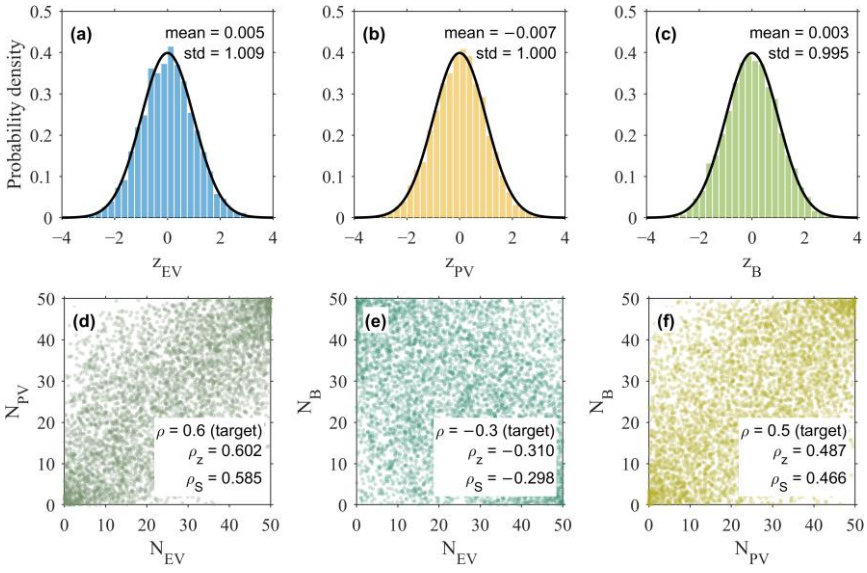


Figure 3. Correlated Monte Carlo samples of DER penetration ($\boldsymbol{N_{MC} = 5000}$): (a–c) marginal distributions of $\boldsymbol{z_{EV}}$, $\boldsymbol{z_{PV}}$, and $\boldsymbol{z_B}$; (d–f) pairwise scatter plots of $\boldsymbol{N_{EV}}$, $\boldsymbol{N_{PV}}$, and $\boldsymbol{N_B}$. $\boldsymbol{\rho}$, $\boldsymbol{\rho_z}$, and $\boldsymbol{\rho_S}$ denote the prescribed, sample, and Spearman rank correlation coefficients, respectively.

2.5. Fuzzy-Based Weighting of Monte Carlo Scenarios

A fuzzy inference system with a Mamdani-type linguistic rule base is employed to assign a duck-curve relevance (DCR) score to each Monte Carlo scenario. EV, PV, and BESS penetration levels are represented by the linguistic terms Low (L), Medium (M), and High (H). The inference consists of fuzzification, rule evaluation with the minimum operator, and defuzzification by the activation-weighted average of singleton consequents.

2.5.1. Fuzzification

For $q \in \{EV, PV, B\}$, the triangular membership function is defined as:

$$\mu(x; a; b; c) = \max\left\{\min\left[\frac{x-a}{b-a}, \frac{c-x}{c-b}\right], 0\right\} \tag{30}$$

For Monte Carlo scenario j, the membership degree corresponding to linguistic level $r \in \{L, M, H\}$ is as follows:

$$\mu_{q,r}^{(j)} = \mu\left(N_q^{(j)}; a_r; b_r; c_r\right) \tag{31}$$

where (a_r, b_r, c_r) are the parameters of the corresponding membership function. The breakpoints of the input membership functions are listed in Table 2. The three inputs share the universe [0, 50] devices and the breakpoints L = (0, 0, 20), M = (10, 25, 40), and H = (30, 50, 50). The peaks lie at the lower bound, the midpoint, and the upper bound of the range, and adjacent terms overlap on [10, 20] and [30, 40], so that every penetration level has a non-zero membership in at least one term and the transitions between terms are gradual.

Table 2. Breakpoints $(\boldsymbol{a}, \boldsymbol{b}, \boldsymbol{c})$ of the triangular input membership functions.

Variable	Universe	L $(\boldsymbol{a}, \boldsymbol{b}, \boldsymbol{c})$	M $(\boldsymbol{a}, \boldsymbol{b}, \boldsymbol{c})$	H $(\boldsymbol{a}, \boldsymbol{b}, \boldsymbol{c})$
EV penetration N_{EV}	[0, 50]	(0, 0, 20)	(10, 25, 40)	(30, 50, 50)
PV penetration N_{PV}	[0, 50]	(0, 0, 20)	(10, 25, 40)	(30, 50, 50)
BESS penetration N_B	[0, 50]	(0, 0, 20)	(10, 25, 40)	(30, 50, 50)

2.5.2. Rule Evaluation

Let $m = 1, \ldots, N_R$ denote the fuzzy-rule index, where $N_R = 27$ is the total number of rules in the complete rule base (Section 2.5.5). For rule m, with antecedent levels (r_{EV}, r_{PV}, r_B), the activation degree for scenario j is as follows:

$$\alpha_m^{(j)} = \min\left\{\mu_{EV,r_{EV}}^{(j)}, \mu_{PV,r_{PV}}^{(j)}, \mu_{B,r_B}^{(j)}\right\} \tag{32}$$

Each rule is assigned a DCR consequent according to the rule base defined in Section 2.5.5.

2.5.3. Singleton Consequents and Defuzzification

Each linguistic DCR term is represented by a singleton at its ordinal value. The consequent of rule m, $D_m \in \{\mathrm{L}, \mathrm{M}, \mathrm{H}\}$, defined by the rule base of Section 2.5.5, is therefore mapped to:

$$d_m = \begin{cases} 1, & D_m = \mathrm{L} \\ 2, & D_m = \mathrm{M} \\ 3, & D_m = \mathrm{H} \end{cases} \tag{33}$$

The DCR score of Monte Carlo scenario j is the activation-weighted average of the rule consequents:

$$DCR_j = \frac{\sum_{\mathrm{m}=1}^{N_R} \alpha_m^{(j)} d_m}{\sum_{\mathrm{m}=1}^{N_R} \alpha_m^{(j)}} \tag{34}$$

2.5.4. Properties of the Relevance Score and Scenario Weighting

The weighted average (34) is the centroid of the singleton output set under sum aggregation and coincides with the output of a zero-order Takagi–Sugeno system with the same rule base, so that no implication or aggregation of continuous output membership functions is required. Because the input partitions overlap and cover the universe [0, 50], at least one rule is active for every sample; the denominator of (34) is therefore positive, and the score is bounded by:

$$1 \le DCR_j \le 3 \tag{35}$$

Consequently, the most relevant sample receives at most three times the weight of the least relevant one. The weighting thus shifts probability mass towards penetration combinations that intensify the duck curve without suppressing the remaining operating conditions, which would otherwise be under-represented in the reduced scenario set. The normalized Monte Carlo weight is as follows:

$$w_j = \frac{DCR_j}{\sum_{\ell=1}^{N_{MC}} D\,CR_\ell} \tag{36}$$

when,

$$\sum_{\ell=1}^{N_{MC}} D\,CR_\ell > 0 \tag{37}$$

Thus,

$$\sum_{j=1}^{N_{MC}} w_j = 1 \tag{38}$$

If all DCR scores are zero, uniform weights are assigned:

$$w_j = \frac{1}{N_{MC}}, j = 1, \ldots, N_{MC} \tag{39}$$

The resulting weights quantify the relative relevance assigned to the sampled DER penetration scenarios by the specified fuzzy rule base.

2.5.5. Complete Fuzzy Rule Base

Each input variable, EV, PV, and BESS penetration, is represented by L, M, and H linguistic levels. Therefore, $N_R = 3^3 = 27$ rules are required.

The DCR consequent is specified by the following matrices for the three BESS levels:

$$\mathcal{D}^{(c)} = \begin{cases} \begin{bmatrix} L & M & H \\ M & H & H \\ H & H & H \end{bmatrix}, & c = L, \\ \begin{bmatrix} L & M & H \\ M & M & H \\ M & H & H \end{bmatrix}, & c = M, \\ \begin{bmatrix} L & M & M \\ M & M & M \\ M & M & H \end{bmatrix}, & c = H. \end{cases} \tag{40}$$

Here, $c \in \{L, M, H\}$denotes the BESS linguistic level, while the rows and columns correspond to the EV and PV levels, respectively. The general rule is as follows:

$$R_{abc}\text{: IF EV} = A_a \text{ AND PV} = B_b \text{ AND BESS} = C_c \text{ THEN DCR} = D_{abc} \tag{41}$$

where $a, b, c \in \{L, M, H\}$, and $D_{abc}$is the corresponding element of $\mathcal{D}^{(c)}$. The fuzzy inference stage therefore converts the sampled DER penetration levels into scenario-specific relevance weights used in the subsequent scenario reduction.

2.6. Probabilistic Scenario Reduction

Direct optimization over all Monte Carlo samples would result in an unnecessarily large computational burden. Therefore, the Monte Carlo samples are reduced to a finite set of representative scenarios.

Let

$$x_j = \left[N_{EV}^{(j)} \quad N_{PV}^{(j)} \quad N_B^{(j)}\right]^T \tag{42}$$

denote the j-th Monte Carlo sample. The samples are clustered into N_K representative groups using K-means clustering. In the case study, N_{MC} = 5000 Monte Carlo samples are reduced to N_K = 10 representative scenarios. The value N_K = 10 was adopted to balance scenario granularity against the computational cost of each fitness evaluation. K-means was run with k-means++ initialization and 5 replicates, and the solution with the lowest within-cluster sum of squares was retained; each centroid is then rounded to the 10-unit penetration resolution. Because a separate schedule is optimized for each scenario, this reduction lowers the number of optimization problems from N_{MC} to N_K, a factor of 500. With N_{pop} = 30 candidates and N_{iter} = 250 iterations per optimization, solving one problem per Monte Carlo sample would require $N_{\text{pop}} \cdot N_{\text{iter}} \cdot N_{MC}$ = 3.75 × 10^7 fitness evaluations, compared with $N_{\text{pop}} \cdot N_{\text{iter}} \cdot N_K$ = 7.5 × 10^4 after the reduction.

For cluster k, the centroid is given by:

$$c_k = \frac{1}{|\mathcal{C}_k|} \sum_{j \in \mathcal{C}_k} x_j \tag{43}$$

where $\mathcal{C}_k$ denotes the set of samples assigned to cluster k. The representative scenario is obtained by mapping each centroid to the prescribed penetration resolution:

$$\xi_k = Q(c_k) \tag{44}$$

where $Q(\cdot)$ denotes the scenario quantization operator.

The probability of representative scenario k is calculated from the fuzzy-weighted Monte Carlo samples belonging to that cluster:

$$p_k = \sum_{j \in \mathcal{C}_k} w_j \tag{45}$$

The probabilities are normalized as:

$$\bar{p}_k = \frac{p_k}{\sum_{\ell=1}^{N_K} p_\ell} \tag{46}$$

such that

$$\sum_{k=1}^{N_K} \bar{p}_k = 1 \tag{47}$$

For notational simplicity, the normalized probability is subsequently denoted by p_k. The resulting representative scenario set is as follows:

$$\mathcal{S} = \{(\xi_k, p_k)\}_{k=1}^{N_K} \tag{48}$$

The resulting scenario set preserves the fuzzy-assigned relevance of the Monte Carlo population while substantially reducing the number of operating conditions considered by the subsequent BESS optimization.

2.7. BESS Scheduling Formulation

2.7.1. Scheduling Decision Variables

The optimization is performed for the critical buses B_C, with $N_C = 6$ as given in (24). The daily horizon is divided into N_B scheduling blocks ($N_B = 12$ blocks of 2 h in the case study). Each block of each BESS is encoded by two bipolar bits, an activity bit and a

direction bit, which together represent the three operating states (charge, idle, and discharge) with binary variables. The number of decision variables is therefore:

$$N_X = 2N_C N_B \tag{49}$$

and the binary decision vector is:

$$X = \left[X_1, X_2, \ldots, X_{N_X}\right]^T \tag{50}$$

with

$$X_l \in \{-1, +1\}, l = 1, \ldots, N_X \tag{51}$$

For critical bus i and scheduling block r, the activity bit $a_{i,r}$ (+1 = active, −1 = inactive) and the direction bit $d_{i,r}$ (+1 = discharge, −1 = charge) are extracted from X as:

$$a_{i,r} = X_{2[(i-1)N_B+r]-1}, \qquad d_{i,r} = X_{2[(i-1)N_B+r]} \tag{52}$$

The three-state block command and the corresponding hourly normalized storage command are:

$$u_{i,r} = \frac{1 + a_{i,r}}{2} d_{i,r} \in \{-1, 0, +1\}, \qquad u_i(t) = u_{i,r},\ t \in T_r \tag{53}$$

where T_r is the set of hours in block r. The direction bit is thus effective only for active blocks, and the command takes one of three values:

$$u_i(t) = -1 \Rightarrow \text{charging}, \quad u_i(t) = 0 \Rightarrow \text{idle}, \quad u_i(t) = +1 \Rightarrow \text{discharging} \tag{54}$$

The factor $(1 + a_{i,r})/2$ equals 0 for an inactive block and 1 for an active block, so (53) maps every pair of bits to a feasible state and every state is reachable by the binary optimizers without additional constraints. In particular, the all-idle vector $\mathbf{X}^{idle}$ ($a_{i,r} = -1$ for all i and r) reproduces the uncontrolled feeder and serves as the no-action reference in (72). The idle state is required because, with a single bit per block (charge or discharge only), every BESS would operate at rated power in every block; a schedule tuned to the high-penetration scenarios was found to increase the ramps of the low-penetration scenarios.

2.7.2. Requested Storage Power

For critical bus i, let $P^B_{i,\max}$ denote the maximum BESS power. The requested storage power is as follows:

$$P_i^{B,\text{req}}(t) = u_i(t) P^B_{i,\max} \tag{55}$$

Positive values denote discharge and negative values denote charging. For an idle block, $u_i(t) = 0$ and therefore $P_i^{B,req}(t) = 0$.

2.7.3. State-of-Charge Dynamics

Let $E_i^{B,\text{rated}}$ denote the rated energy capacity of the storage unit and $SOC_i(t)$ represents its normalized state of charge, subject to:

$$SOC_i^{\min} \le SOC_i(t) \le SOC_i^{\max} \tag{56}$$

During discharge,

$$SOC_i(t+1) = SOC_i(t) - \frac{P_i^B(t)}{\eta_{i,d} E_i^{B,\text{rated}}}, P_i^B(t) > 0 \tag{57}$$

where $\eta_{i,d}$ is the discharge efficiency. The maximum feasible discharge power is as follows:

$$P_{i,d}^{B,\max}(t) = \eta_{i,d}\left[SOC_i(t) - SOC_i^{\min}\right] E_i^{B,\text{rated}} \tag{58}$$

Thus, the actual discharge power is expressed as:

$$P_i^B(t) = \min\left[P_i^{B,\mathrm{req}}(t), P_{i,d}^{B,\max}(t)\right] \tag{59}$$

During charging,

$$SOC_i(t+1) = SOC_i(t) + \frac{|\, P_i^B(t)\,|\,\eta_{i,c}}{E_i^{B,\mathrm{rated}}} \tag{60}$$

where $\eta_{i,c}$ is the charging efficiency. The available charging energy is as follows:

$$E_{i,c}^{B,\mathrm{avail}}(t) = [SOC_i^{\max} - SOC_i(t)]E_i^{B,\mathrm{rated}} \tag{61}$$

giving the maximum grid-side charging power as:

$$P_{i,c}^{B,\max}(t) = \frac{E_{i,c}^{B,\mathrm{avail}}(t)}{\eta_{i,c}} \tag{62}$$

Consequently,

$$P_i^B(t) = -\min\left[\left|P_i^{B,\mathrm{req}}(t)\right|, P_{i,c}^{B,\max}(t)\right] \tag{63}$$

These relations keep the requested BESS operation within the nominal power and energy limits of the storage model. In the optimization, the SOC and the BESS parameters are taken as known; the effect of their measurement uncertainty is evaluated in Section 4.7, whereas the sub-hourly dynamic response of the BESS is not represented. In the idle state, $P_i^B(t) = 0$ and the SOC is unchanged, $SOC_i(t+1) = SOC_i(t)$.

2.8. Probabilistic Substation Power Model

Each representative scenario k is defined by its penetration vector (64) and its device set (65), and its uncontrollable substation profile (66) is obtained from a 24-h quasi-static time-series power flow of the feeder $\mathcal{G}$ with the devices $\mathcal{D}_k$, computed with OpenDSS:

$$\mathrm{s}_k = \left[N_{EV,k},\ N_{PV,k},\ N_{B,k}\right] \tag{64}$$

$$\mathcal{D}_k = \mathcal{D}_{1:N_{EV,k}}^{EV} \cup \mathcal{D}_{1:N_{PV,k}}^{PV} \cup \mathcal{D}_{1:N_{B,k}}^{B} \tag{65}$$

$$P_k^{base}(t) = \mathcal{P}_t\,(\mathcal{G}, \mathcal{D}_k), \quad t \in T \tag{66}$$

where the device sets are nested subsets of one fixed fleet of EVs, PV units, and customer BESSs generated once with a fixed random seed, so that two scenarios differ only in the number of connected devices and not in their random profiles. The customer BESSs are part of $\mathcal{D}_k$ and are not optimized. The circuit is rebuilt from a clean state before each scenario. The critical scenario used in Section 2.3 and in the performance evaluation is the penetration combination with the steepest baseline ramp:

$$\mathrm{s}^* = \arg\max_{\mathrm{s}\in\mathcal{S}_{grid}} \max_t |P_{\mathrm{s}}^{base}(t+1) - P_{\mathrm{s}}^{base}(t)| \tag{67}$$

where $\mathcal{S}_{grid} = \{0,10,\ldots,50\}^3$ contains the 216 combinations of EV, PV, and customer-BESS counts. The six optimized BESSs at the critical buses are dedicated units that are available in every scenario. Because a single schedule cannot suit both high- and low-penetration days, a separate day-ahead schedule $\mathbf{X}_k$ is optimized for each representative scenario k and for the critical scenario (Section 3.3); in operation, the schedule of the scenario that matches the day-ahead forecast of EV, PV, and BESS penetration is applied. The aggregate power of the six BESSs under schedule $\mathbf{X}_k$ is:

$$P_k^B(t) = \sum_{i\in B_C} P_i^B\ (t;\, \mathrm{X}_k) \tag{68}$$

Using the adopted sign convention, the substation power of scenario k evaluated in the fitness function is:

$$P_k^{sub}(t) = P_k^{base}(t) - P_k^B(t) \tag{69}$$

Discharging therefore reduces the power drawn from the upstream substation, whereas charging increases it. Each optimized schedule is subsequently validated in OpenDSS in its own scenario, where each optimized BESS is represented by a constant-power element at its critical bus that follows its SOC-feasible schedule:

$$\hat{P}_k^{sub}(t) = \mathcal{P}_t\left(\mathcal{G}, \mathcal{D}_k \cup \{P_i^B(t; \mathrm{X}_k)\}_{i\in B_C}\right) \tag{70}$$

The convergence of every hourly solution is checked. The difference between the validated and the modeled profiles,

$$\varepsilon_k = \max_{t\in T}\left|\hat{P}_k^{sub}(t) - P_k^{sub}(t)\right| \tag{71}$$

reflects the change in feeder losses and voltage-regulator tap positions caused by the BESS power; it remained within about one BESS rating in all validations. All duck-curve indices in Section 4 are therefore computed from the validated profiles. The expected objective of the all-idle schedule defines the no-action reference:

$$J^{ref} = \sum_{k=1}^{N_K} p_k\, J_k^{tot}\,(\mathrm{X}^{idle}), \quad a_{i,r} = -1 \;\; \forall\, i \in B_C,\; r = 1, \ldots, N_B \tag{72}$$

where $\mathbf{X}^{idle}$ reproduces the uncontrolled feeder in every scenario and J_k^{tot} is defined in (95). The objective reduction of an algorithm is expressed as $100\,(J^{ref} - J^{exp})/J^{ref}$, with J^{exp} from (90).

3. Probabilistic Duck-Curve Objective and BESS Optimization

3.1. Probabilistic Duck-Curve Objective Function

The duck-curve characteristics of the substation power profile are quantified using four complementary aspects: maximum power ramp, peak-to-valley range, midday depression, and evening variation. These metrics are evaluated for each representative scenario and subsequently combined into a probabilistic objective.

3.1.1. Duck-Curve Metrics

Maximum Ramp

For scenario k, the maximum hourly variation in substation power is defined as:

$$R_k = \max_{t=1,\ldots,N_T-1}\left|P_k^{\mathrm{sub}}(t+1) - P_k^{\mathrm{sub}}(t)\right| \tag{73}$$

This metric represents the largest hour-to-hour change in substation power over the considered time horizon and is used to quantify the severity of rapid power fluctuations.

Peak-to-Valley Range

The maximum and minimum substation power values for scenario $k$are defined as:

$$P_k^{\max} = \max_{t\in\mathcal{T}} P_k^{sub}(t) \tag{74}$$

$$P_k^{\min} = \min_{t\in\mathcal{T}} P_k^{sub}(t) \tag{75}$$

The daily peak-to-valley range is as follows:

$$D_k = P_k^{\max} - P_k^{\min} \tag{76}$$

This metric quantifies the overall variation in substation power between its daily peak and valley values and therefore provides a measure of the magnitude of the duck-curve profile.

Midday Shape Metric

Let T_M denote the predefined midday interval. The average substation power during this interval is calculated as:

$$P_k^{mid} = \frac{1}{|\mathcal{T}_M|} \sum_{t \in \mathcal{T}_M} P_k^{sub}(t) \tag{77}$$

The midday shape metric is then defined as:

$$M_k = \left(P_k^{\max} - P_k^{mid}\right)^2 + \left(P_k^{\min} - P_k^{mid}\right)^2 \tag{78}$$

This metric measures the deviation of the midday average power from the daily peak and valley levels, thereby capturing the characteristic midday depression associated with the duck-curve phenomenon.

Evening Ramp

Let T_E denote the predefined evening interval. The maximum substation power ramp within this interval is defined as:

$$R_{k,E} = \max_{t \in \mathcal{T}_E} |P_k^{sub}(t+1) - P_k^{sub}(t)| \tag{79}$$

In addition, the evening-rise penalty is formulated as:

$$E_k = \left[P_k^{sub}(t_E^{end}) - P_k^{sub}(t_E^{start})\right]_+^2 \tag{80}$$

where

$$[x]_+ = \max\{x, 0\} \tag{81}$$

and t_E^{start} and t_E^{end} denote the beginning and end of the predefined evening interval, respectively. The evening-ramp metric captures the maximum short-term variation during the evening period, whereas the evening-rise penalty quantifies the magnitude of the net increase in substation power across the interval. The midday-shape metric (78) and the evening-rise penalty (80) use squared deviations because the operational burden of the duck curve grows faster than linearly with the deviation: a deep valley or a large evening rise determines the required ramping and reserve capacity, whereas small deviations are absorbed by regular control. Squaring penalizes one large excursion more than several small excursions of equal total magnitude and thus steers the search away from schedules that leave a single severe deviation. Because the profiles are simulated rather than measured, large deviations are genuine operating features rather than outliers. Normalization by P_{scale}^2 in (85) and (87) keeps the squared terms commensurate with the linear worst-case metrics (73), (76), and (79), which are retained.

3.1.2. Objective Normalization

To avoid domination of the objective by differences in physical units and magnitudes, the quantities are normalized with one substation-power scale common to all scenarios:

$$P_{scale} = \max_{k,\, t \in T} \left|P_k^{base}(t)\right| + \epsilon \tag{82}$$

where $\epsilon > 0$ is a small numerical constant.

The normalized metrics are as follows:

$$\bar{R}_k = \frac{R_k}{P_{scale}} \tag{83}$$

$$\bar{D}_k = \frac{D_k}{P_{scale}} \tag{84}$$

$$\bar{M}_k = \frac{M_k}{P_{scale}^2} \tag{85}$$

$$\bar{R}_{k,E} = \frac{R_{k,E}}{P_{scale}} \tag{86}$$

and,

$$\bar{E}_k = \frac{E_k}{P_{scale}^2} \tag{87}$$

3.1.3. Probabilistic Duck-Curve Fitness

The scenario-specific objective is defined as:

$$J_k = \omega_R \bar{R}_k + \omega_D \bar{D}_k + \omega_M \bar{M}_k + \omega_E \bar{R}_{k,E} + \omega_{ER} \bar{E}_k \tag{88}$$

where

$$\omega_R + \omega_D + \omega_M + \omega_E + \omega_{ER} = 1 \tag{89}$$

Each representative scenario k receives its own optimized schedule $\mathbf{X}_k^*$ (Section 3.3). The probabilistic performance of the framework is the expected objective of these schedules over the reduced scenario set:

$$J^{exp} = \sum_{k=1}^{N_K} p_k \, J_k^{tot} \, (\mathrm{X}_k^*) \tag{90}$$

where J_k^{tot} is the complete scenario objective defined in (95). The same weights $\omega_R = 0.40$, $\omega_D = 0.20$, $\omega_M = 0.20$, $\omega_E = 0.15$, and $\omega_{ER} = 0.05$ are used for all scenarios.

3.1.4. Storage-Usage and Terminal-SOC Regularization

To limit unnecessary storage activity, a storage-utilization regularization term is introduced. The normalized storage utilization is as follows:

$$U_B = \frac{1}{N_C N_T} \sum_{i \in B_C} \sum_{t \in T} \frac{| P_i^B(t) |}{P_{i,\max}^B} \tag{91}$$

The corresponding regularization term is as follows:

$$J_{\mathrm{reg}} = \lambda_{\mathrm{reg}} U_B \tag{92}$$

where $\lambda_{\mathrm{reg}}$is a weighting parameter. The terminal SOC deviation is calculated as:

$$D_{\mathrm{SOC}} = \frac{1}{N_C} \sum_{i \in B_C} |SOC_i(N_T + 1) - SOC_i(1)| \tag{93}$$

The corresponding terminal-SOC penalty is represented as follows:

$$J_{\mathrm{SOC}} = \lambda_{\mathrm{SOC}} D_{\mathrm{SOC}} \tag{94}$$

The complete objective of scenario k, minimized by the optimizer, is therefore:

$$J_k^{tot}(\mathrm{X}) = J_k(\mathrm{X}) + J_{reg}(\mathrm{X}) + J_{SOC}(\mathrm{X}) \tag{95}$$

The resulting physical storage power and SOC satisfy the following:

$$-P_{i,\max}^B \le P_i^B(t) \le P_{i,\max}^B \tag{96}$$

and

$$SOC_i^{\min} \le SOC_i(t) \le SOC_i^{\max} \tag{97}$$

The resulting formulation provides the probabilistic objective evaluated by the IBiEO optimizer while maintaining feasible BESS operation across the considered DER scenarios. Because the idle state is available, the storage-utilization term (92) is no longer a constant offset: it favours idle blocks whenever charging or discharging does not reduce the duck-curve objective. The weights used in the case study are $\lambda_{reg} = 0.001$ and $\lambda_{SOC} = 0.01$.

3.2. Improved Binary Equilibrium Optimizer (IBiEO)

The scheduling problem of Section 2.7 is solved with an improved binary Equilibrium Optimizer (IBiEO). The underlying Equilibrium Optimizer (EO) is a population-based metaheuristic that updates candidate solutions toward an equilibrium pool of promising solutions [44]; binary variants map the continuous EO update to bit decisions through transfer functions [45]. I The EO was originally validated on 58 benchmark functions and three engineering problems against GA, PSO, GWO, GSA, SSA, CMA-ES, SHADE, and LSHADE-SPACMA [44]. In the present study, each bit of $\mathbf{X}$ is a bipolar activity or direction bit of one BESS in one scheduling block (Section 2.7.1). In a direct binary implementation of EO (BiEO), the equilibrium pool is built from the current population only, every updated position is accepted, and a triggered bit is redrawn at random; in preliminary tests, this implementation was outperformed by several of the benchmark algorithms, which motivates four modifications:

i. Memory-based equilibrium pool: the pool holds the four best distinct solutions found so far, as in the continuous EO [39], rather than the four best members of the current population, so that good schedules are not lost between iterations (110b).
ii. Particle memory saving (greedy selection): an agent moves to its trial position only if the objective does not deteriorate (110a), which is the memory-saving step of the continuous EO [39] applied to bipolar vectors.
iii. Generation-rate term and bit-flip mapping: the generation-rate term (103)–(105) with GP = 0.5 enters the concentration update, and a triggered bit is inverted (−1 ↔ +1) rather than redrawn at random, so that every triggered transition changes the state (110).
iv. Diversity control: each bit is additionally flipped with the mutation probability $p_m = 1/N_X$ in (108), and if the best objective has not improved for 15 consecutive iterations, the worse half of the population is re-initialized at random while the equilibrium pool is retained.

Modifications (i) and (ii) and the generation-rate term are taken from the continuous EO [44] and adapted to the bipolar decision space; the bipolar three-state encoding, the bit-flip mapping, the uniform bit-flip mutation, and the stagnation-triggered restart are introduced in this work. Both versions use N_{pop} fitness evaluations per iteration, so the modifications do not increase the evaluation budget. Because the optimizer is applied here to a specific engineering problem, its performance is assessed directly on the BESS scheduling problem against five binary algorithms (Section 4). According to the no-free-lunch theorem [46], rankings obtained on benchmark suites do not transfer reliably to a particular application.

3.2.1. Equilibrium-Based Search

Let the n-th IBiEO candidate be represented by the concentration vector Y_n. The initial population is generated within the prescribed search bounds as:

$$Y_n^0 = Y_{\min} + \zeta_n(Y_{\max} - Y_{\min}), n = 1,2, \dots, N_{\text{pop}} \tag{98}$$

where $Y_n^0$is the initial concentration vector of candidate n, $Y_{\min}$and $Y_{\max}$are the lower and upper concentration bounds, respectively, and $\zeta_n$is a random vector whose elements are uniformly distributed over $[0, 1]$. In IBiEO, the four best distinct candidates found up to the current iteration are selected together with their arithmetic mean to construct the equilibrium pool:

$$\mathcal{E} = \{Y_{e,1}, Y_{e,2}, Y_{e,3}, Y_{e,4}, Y_{e,\text{avg}}\} \tag{99}$$

where

$$Y_{e,\text{avg}} = \frac{1}{4}\sum_{a=1}^{4} Y_{e,a} \quad (100)$$

For each candidate, one member of $\mathcal{E}$ is selected as the reference equilibrium vector. This equilibrium pool provides the reference states toward which the candidate concentrations are updated. The exponential coefficient controlling the equilibrium-based movement is defined as:

$$\Psi = a_1 \operatorname{sign}\left(\rho - \frac{1}{2}\right)[e^{-\chi\tau} - 1] \quad (101)$$

where $a_1$is a control parameter, $\rho$and $\chi$are independent random vectors with elements uniformly distributed over $[0, 1]$, and $\tau$is the normalized iteration parameter given by:

$$\tau = \left(1 - \frac{\nu}{N_{\text{iter}}}\right)^{\frac{a_2\nu}{N_{\text{iter}}}} \quad (102)$$

where νdenotes the current IBiEO iteration, $N_{\text{iter}}$is the maximum number of iterations, and $a_2$is a control parameter. EO also employs a generation-rate mechanism to improve the refinement of promising solutions. The generation-rate vector is expressed as:

$$\Gamma = \Gamma_0\Psi \quad (103)$$

where

$$\Gamma_0 = \Omega(Y_e - \chi Y) \quad (104)$$

and the generation-control coefficient is as follows:

$$\Omega = \begin{cases} 0.5\rho_1, & \rho_2 \geq GP, \\ 0, & \rho_2 < GP, \end{cases} \quad (105)$$

where $\rho_1$and $\rho_2$are independently generated random numbers in $[0, 1]$, $GP$is the generation probability, and Ωcontrols the contribution of the generation-rate mechanism. The continuous EO concentration update is then expressed as:

$$Y^+ = Y_e + (Y - Y_e)\Psi + \frac{\Gamma}{\chi V}(1 - \Psi) \quad (106)$$

where $V$is the volume parameter used in the EO formulation. In the case study, $a_1 = 2$, $a_2 = 1$, and $GP = 0.5$.

3.2.2. Binary Mapping and BESS Scheduling

Because the scheduling variables in Section 2.7 are binary, the continuous equilibrium update is converted into a bit-transition probability. In IBiEO, the bipolar position $\mathbf{X}_n$ of agent n plays the role of Y in (106), and the concentration variation is defined as the difference between the continuous EO update Y^+ and the current position:

$$\Delta Y = Y^+ - Y \quad (107)$$

In addition to the transfer-function trigger, every bit is flipped with the mutation probability:

$$p_m = \frac{1}{N_X} \quad (108)$$

The magnitude of the concentration variation is mapped to a bit-flipping probability using the V-shaped transfer function:

$$\Pi(\Delta Y) = \left|\frac{2}{\pi}\tan^{-1}\left(\frac{\pi}{2}\Delta Y\right)\right| \quad (109)$$

For bit d of agent n, the trial state is obtained by flipping the bit when the transfer function or the mutation is triggered:

$$\tilde{X}_{n,d} = \begin{cases} -X^{\nu}_{n,d}, & \rho^{(1)}_{n,d} < \Pi^{\nu}_{n,d} \text{ or } \rho^{(2)}_{n,d} < p_m \\ X^{\nu}_{n,d}, & \text{otherwise} \end{cases} \quad (110)$$

where $\rho^{(1)}_{n,d}$ and $\rho^{(2)}_{n,d}$ are independent random numbers uniformly distributed on [0, 1]. The trial vector is accepted only if it does not deteriorate the objective (particle memory saving):

$$\mathrm{X}^{\nu+1}_{n} = \begin{cases} \widetilde{\mathrm{X}}_{n}, & J\left(\widetilde{\mathrm{X}}_{n}\right) \le J\left(\mathrm{X}^{\nu}_{n}\right) \\ \mathrm{X}^{\nu}_{n}, & \text{otherwise} \end{cases} \quad (111)$$

and the equilibrium pool keeps the four best distinct solutions found so far:

$$\mathrm{E}^{\nu+1} = \mathrm{best}_4\left(\mathrm{E}^{\nu} \cup \{\widetilde{\mathrm{X}}_1, \ldots, \widetilde{\mathrm{X}}_{N_{pop}}\}\right) \quad (112)$$

where $\mathrm{best}_4(\cdot)$ returns the four distinct vectors with the lowest objective values. If the best objective value has not improved for 15 consecutive iterations, the worse half of the population is re-initialized at random and evaluated; the pool is kept. The overall procedure is summarized in Figure 4. A V-shaped rather than an S-shaped transfer function is used for three reasons. First, (109) yields a flip probability that vanishes at $\Delta Y = 0$, so a candidate that coincides with its equilibrium reference retains its bits, whereas an S-shaped function returns 0.5 and keeps re-randomizing converged bits. Second, the V-shaped rule inverts a bit relative to its current value instead of forcing it to a value determined by the sign of ΔY, which is consistent with the symmetric bipolar encoding (51)–(53), in which neither value of an activity or direction bit is preferred. Third, V-shaped functions have been shown to provide stronger exploitation and less stagnation than S-shaped functions in binary metaheuristics [47].

3.2.3. Computational Complexity

Let N_{pop}, N_{iter}, and $N_X = 2N_C \cdot N_B$ denote the population size, the number of iterations, and the number of binary variables, and let C_f be the cost of one fitness evaluation. Evaluating (95) requires the SOC propagation over N_C buses and N_T hours and the duck-curve metrics of one profile, so $C_f = O(N_T \cdot N_C)$; the OpenDSS baselines are computed once beforehand and do not contribute to C_f. Per iteration, IBiEO additionally updates the memory pool and evaluates (101)–(110), both $O(N_{\mathrm{pop}} \cdot N_X)$, and forms the average candidate, $O(N_X)$. One optimization therefore requires $O(N_{\mathrm{iter}} \cdot N_{\mathrm{pop}} \cdot (N_X + N_T \cdot N_C))$ time and $O(N_{\mathrm{pop}} \cdot N_X)$ memory, the same order as BPSO and the other binary benchmarks. A complete schedule table requires $N_K + 1$ independent optimizations, which can be executed in parallel; in the case study, $N_X = 144$, $N_K = 10$, $N_T = 24$, and $N_C = 6$.

All algorithms used $N_{\mathrm{pop}} = 30$, $N_{\mathrm{iter}} = 250$, and a hard budget of 7500 fitness evaluations per optimization, enforced by a counter that returns a penalty once the budget is exhausted. They solved identical problems (device fleet, scenarios, baselines, and critical buses), and run r of every algorithm used the same random seed for each scenario. All algorithms consumed the full budget except BDMO, which used 7023 evaluations on average within the same number of iterations. The mean time per optimization, excluding the OpenDSS validation, was 1.49 s for IBiEO and 1.53–3.40 s for the benchmarks (16.4 s for all 11 optimizations of IBiEO) on an Intel Core i7-4930K CPU (3.4 GHz; Intel Corporation, Santa Clara, CA, USA) with 32 GB RAM under Windows 10 Home (Microsoft

Corporation, Redmond, WA, USA) and MATLAB R2024a (The MathWorks, Inc., Natick, MA, USA). After 30 iterations, IBiEO already attains 0.0412, close to the final mean objective of BPSO (0.0408) (Section 4.4); its advantage therefore does not result from additional evaluations.

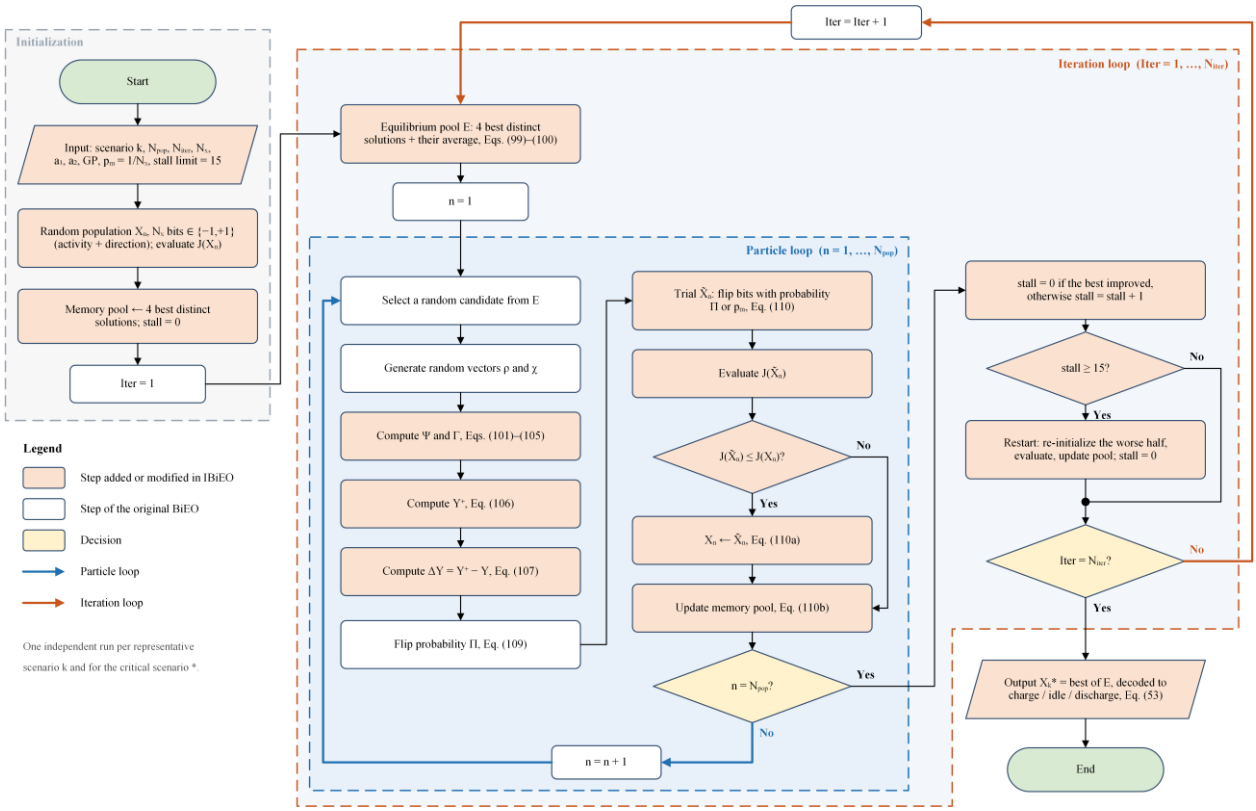


Figure 4. Flowchart of the proposed IBiEO. Shaded steps denote the modifications to the original BiEO.

3.3. The Proposed Optimization Problem

The IBiEO algorithm optimizes the binary scheduling vector X defined in (50)–(53). Each candidate binary vector specifies the charging, idle, or discharging state of the BESSs at the selected critical buses over the predefined scheduling blocks. For each candidate solution, the corresponding physical BESS power is obtained from the SOC-constrained relations in (55)–(63), and the resulting storage schedule is evaluated in the scenario for which it is optimized. One optimization problem is solved for each representative scenario of Section 2.6 and for the critical scenario (denoted *):

$$\mathrm{X}_k^* = \underset{\mathrm{X}}{\operatorname{argmin}}\, J_k^{tot}(\mathrm{X}), \quad k \in \{1, \ldots, N_K\} \cup \{*\} \tag{113}$$

subject to

$$X_l \in \{-1, +1\}, \; l = 1, \ldots, N_X \tag{114}$$

$$-P_{i,\max}^B \le P_i^B(t) \le P_{i,\max}^B, \; i \in B_C, \; t \in T \tag{115}$$

and

$$SOC_i^{\min} \le SOC_i(t) \le SOC_i^{\max}, \; i \in B_C, \; t \in T \tag{116}$$

Here, $J(X)$is the complete objective of scenario k defined in (95), comprising the duck-curve objective, storage-utilization regularization, and terminal-SOC penalty. For each candidate X, the corresponding BESS schedule is propagated through the SOC dynamics, and the substation-power profile of the scenario is calculated using (69). The resulting profile is then used to evaluate the duck-curve objective (88) together with the regularization terms in (92) and (94). The optimization therefore determines a three-state BESS operating schedule that minimizes the duck-curve severity of each representative DER scenario while limiting unnecessary storage utilization and terminal SOC deviation. The best feasible candidate identified by IBiEO is retained as the optimized scheduling solution and is subsequently evaluated using the performance measures defined in Section 3.5. The resulting set of schedules forms a day-ahead schedule table; the schedule of the scenario that best matches the day-ahead forecast is applied, and the expected performance of the table is given by (90).

3.4. Overall Proposed Algorithm

The sequential implementation of the proposed framework is summarized in Algorithm 1. The procedure begins with correlated DER scenario generation and scenario relevance assessment, followed by scenario reduction and critical-bus identification. The resulting representative scenarios and selected BESS locations are then used in the probabilistic IBiEO-based scheduling process implemented in MATLAB. The optimized schedules are subsequently evaluated through automated 24-h time-series distribution-system simulations in OpenDSS using the MATLAB–COM interface. The resulting substation power profiles are then used to quantify the duck-curve performance and validate the effectiveness of the proposed framework.

Algorithm 1: Overall procedure of the Proposed Probabilistic BESS Scheduling Framework

Input: Distribution-network model; hourly load, PV, and EV profiles; penetration ranges of PV, EV, and BESS; prescribed correlation coefficients; BESS technical limits; fuzzy-rule base; number of Monte Carlo samples N_{MC}; number of clusters N_K; IBiEO parameters.
Output: Table of optimized BESS charging/idle/discharging schedules, one per scenario, and corresponding substation-power profile.

1. Initialize the distribution system.

Load the IEEE 34-bus distribution-system model and define the residential aggregation buses, load profiles, PV generation, EV charging profiles, and BESS parameters. Define the 24-h simulation horizon and the BESS power, energy, SOC, and operating constraints.

2. Identify candidate BESS locations.

Simulate the 216 penetration combinations, select the critical scenario with the steepest substation ramp (67), and perform its baseline time-series power-flow simulation without optimized BESS operation. Calculate the temporal power-variability index for each non-source bus and rank the buses according to their variability. Select the buses with the highest variability as the critical BESS control locations.

3. Generate correlated DER scenarios.

Construct the correlation matrix for PV, EV, and BESS penetration levels. Generate correlated Gaussian random samples using the prescribed dependence structure. Transform the samples through the standard-normal cumulative distribution function and map them to the specified DER penetration ranges to obtain N_{MC}joint operating scenarios.

4. Evaluate scenario relevance.

For each Monte Carlo scenario, apply the fuzzy inference system using the PV, EV, and BESS penetration levels as inputs. Perform fuzzification and rule evaluation, and

compute the activation-weighted average of the singleton rule consequents to obtain the duck-curve relevance (DCR) score of each scenario.

5. Assign scenario weights.

Normalize the DCR scores to obtain the probability weight associated with each Monte Carlo scenario.

6. Reduce the scenario set.

Apply K-means clustering to the generated Monte Carlo scenarios. For each cluster, determine the centroid and map it to the prescribed penetration resolution. Calculate the representative-scenario probability from the normalized fuzzy weights of the samples belonging to each cluster. The resulting set contains N_K representative operating scenarios.

7. Define the probabilistic BESS scheduling problem.

Construct the binary scheduling vector with one activity bit and one direction bit per critical bus and scheduling block, and decode it into charge, idle, or discharge commands (53). For each candidate schedule, determine the feasible BESS charging, idle, or discharging power and update the SOC while enforcing BESS power and energy constraints.

8. Evaluate each candidate schedule across representative scenarios.

Compute the baseline substation profile of every representative scenario and of the critical scenario once with OpenDSS (66). For each candidate schedule of scenario k, propagate it through the SOC-constrained storage model and subtract the aggregate BESS power from the baseline profile of scenario k (68)–(69).

9. Calculate the probabilistic objective.

For the scenario being optimized, calculate the normalized maximum ramp, peak-to-valley range, midday depression, and evening variation. Combine these metrics according to the prescribed objective weights (88). Add the storage-utilization regularization and terminal-SOC penalty to obtain the complete fitness value.

10. Optimize the BESS schedule using BiEO.

For each scenario k, initialize the IBiEO population with random bipolar vectors and maintain the memory pool of the four best distinct solutions and their mean. Update each agent with the equilibrium and generation-rate terms, map the variation to flip probabilities with the V-shaped transfer function, apply bit flips and mutation, and accept the trial vector only if it does not deteriorate the objective. Re-initialize the worse half of the population after 15 iterations without improvement.

11. Check feasibility and update the optimum.

For each updated candidate, enforce the BESS power and SOC constraints and evaluate its probabilistic objective. Retain the best feasible candidate and repeat the IBiEO update process until the evaluation budget $N_{\text{pop}} \cdot N_{\text{iter}}$ is exhausted.

12. Obtain the optimized schedule

For each scenario, select the best feasible IBiEO solution as the final BESS charging/idle/discharging schedule for the critical buses. The day-ahead forecast selects which schedule of the table is applied.

13. Perform time-series validation.

Implement each optimized BESS schedule in the distribution-system model of its scenario as six constant-power elements following the SOC-feasible schedule (70), and perform 24-h time-series power-flow simulations. Check the convergence of every hourly solution and obtain the resulting substation power.

14. Evaluate performance

Compare the optimized and baseline substation-power profiles using the maximum ramp and peak-to-valley range, together with the other defined duck-curve indices. Calculate the corresponding percentage improvements.

15. Statistical validation.

Repeat the optimization for multiple independent runs and compare IBiEO with the benchmark algorithms under the same evaluation budget and random seeds using appropriate statistical tests to assess the significance and repeatability of the obtained optimization results.

End Algorithm

3.5. Performance Evaluation

The performance of the optimized schedule is evaluated by comparing the original and optimized substation-power trajectories. The original maximum ramp is:

$$R_{orig} = \max_{t=1,\ldots,N_T-1} |P_{sub,orig}(t+1) - P_{sub,orig}(t)| \quad (117)$$

whereas the optimized maximum ramp is as follows:

$$R_{opt} = \max_{t=1,\ldots,N_T-1} |P_{sub,opt}(t+1) - P_{sub,opt}(t)| \quad (118)$$

The percentage change in maximum ramp is computed as:

$$\Delta R(\%) = \frac{R_{orig} - R_{opt}}{\max\{R_{orig}, \epsilon\}} \times 100 \quad (119)$$

Similarly, the original and optimized peak-to-valley ranges are:

$$D_{orig} = \max_{t\in\mathcal{T}} P_{sub,orig}(t) - \min_{t\in\mathcal{T}} P_{sub,orig}(t) \quad (120)$$

$$D_{opt} = \max_{t\in\mathcal{T}} P_{sub,opt}(t) - \min_{t\in\mathcal{T}} P_{sub,opt}(t) \quad (121)$$

The corresponding change in peak-to-valley range is:

$$\Delta D(\%) = \frac{D_{orig} - D_{opt}}{\max\{D_{orig}, \epsilon\}} \times 100 \quad (122)$$

These metrics quantify the change in the maximum substation ramp and peak-to-valley range resulting from the coordinated BESS schedule.

4. Results and Discussion

The proposed IBiEO is compared with five binary benchmark algorithms: the Binary Detective Behavior Algorithm (BDBA), Binary Dragonfly Algorithm (BDA), Binary Dwarf Mongoose Optimizer (BDMO), Binary Particle Swarm Optimization (BPSO), and a hybrid of the Detective Behavior Algorithm and Particle Swarm Optimization (DBA-PSO). All six algorithms solve the identical problems defined in Sections 2 and 3: one fixed device fleet, the ten representative scenarios of Section 2.6 with their OpenDSS baselines and the critical scenario $s^* = (50,50,0)$, the six critical buses of Section 2.3, the three-state encoding with $N_X = 144$, $N_{pop} = 30$, a budget of 7500 fitness evaluations per optimization, and 30 independent runs with seeds shared across algorithms. In each run, every algorithm optimizes 11 schedules (ten representative scenarios and the critical scenario). All duck-curve indices are computed from OpenDSS validations, and each scenario is compared with its own uncontrolled profile.

4.1. Substation Power Profiles

Figure 5 compares the uncontrolled substation profile of the critical scenario with the mean of the 30 validated profiles of each algorithm. The uncontrolled profile reaches a morning peak of 1.99 MW at hour 7, falls to a midday valley of about 1.56 MW over hours

12–15, and rises to an evening peak of 2.31 MW at hour 19; the steepest ramp, 266.2 kW, occurs between hours 18 and 19, and the peak-to-valley range is 752.1 kW. These features originate largely at the six critical buses identified in Section 2.3, namely mid806, 860, mid846, mid848, mid828, and mid822 (Figure 2). The devices at these buses produce 57.4% of the substation evening rise (431.8 of 752.1 kW over hours 15–19) and 48.2% of the steepest hourly ramp (128.4 of 266.2 kW), while their largest hourly swing of 148.2 kW remains within the 300-kW aggregate rating of the optimized BESSs. The critical buses therefore constitute the dominant source of the substation duck curve, and the installed BESS power is sufficient to offset their variation. Complete compensation of their net demand would remove about 48% of the steepest ramp, which bounds the ramp reduction attainable by acting on these buses alone. All optimized schedules reshape the profile in the same way: they lower the night and morning hours, raise the midday valley to about 1.63–1.66 MW, and flatten the evening peak to about 2.06–2.07 MW. For IBiEO, the evening peak of the mean profile decreases from 2.31 MW to 2.06 MW, the valley rises from 1.56 MW to 1.66 MW, and the largest hourly ramp decreases from 266.2 kW to 120.8 kW. The profiles of IBiEO, DBA-PSO, BDMO, BDA, and BPSO nearly coincide in this scenario, whereas BDBA leaves a visibly higher evening peak (2.14 MW). The evening peak is limited by the 300-kW total BESS rating and by the share of the critical buses in the evening rise.

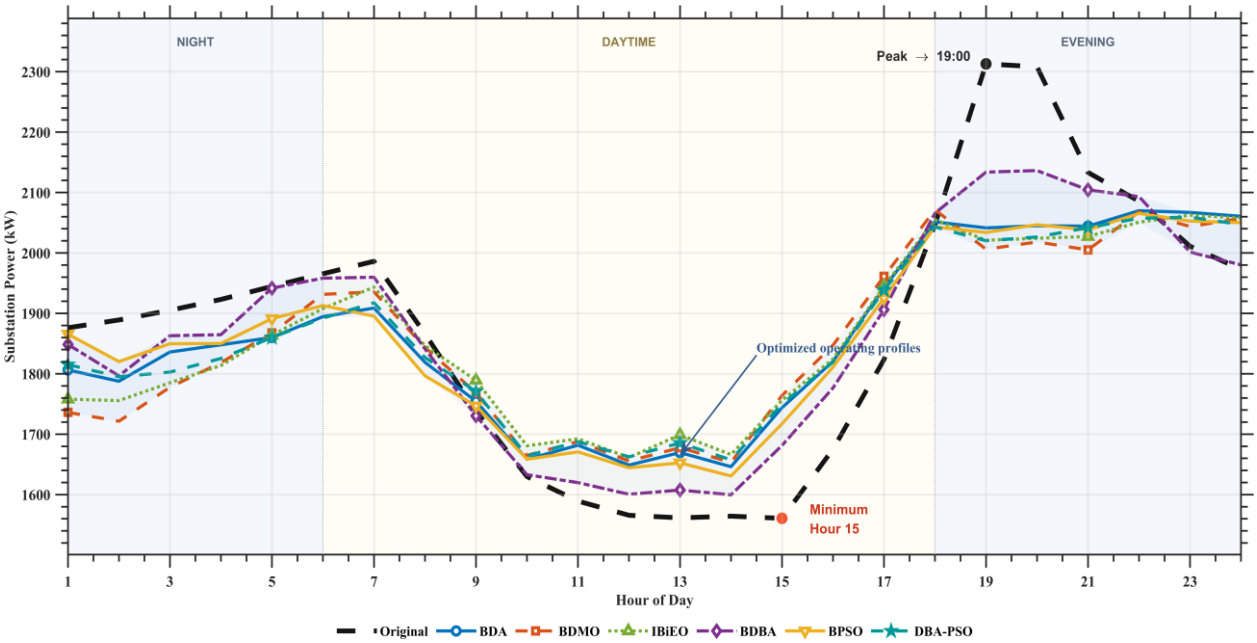


Figure 5. Substation power profiles in the critical scenario s^* = (50, 50, 0): uncontrolled feeder and mean validated profiles of the six algorithms over 30 runs.

4.2. Hourly Energy-Storage Operations

Figure 6 shows the hourly substation-power reduction in the critical scenario for the run of each algorithm with the lowest critical-scenario objective; positive values correspond to discharging and negative values to charging. All algorithms discharge during the night, the morning, and the evening peak (hours 19–21) and charge during the midday valley (hours 9–17). IBiEO achieves the largest reduction, 360.9 kW at hour 19, against 297.5–314.8 kW for BDA, BDMO, BPSO, and DBA-PSO and 238.7 kW for BDBA, and its largest charging power, about 220 kW at hour 15, raises the valley. Over all runs and representative scenarios, the BESSs are active in about 33% of the BESS-hours for IBiEO (32–35% for the benchmarks) and idle otherwise, which confirms that the idle state is used extensively.

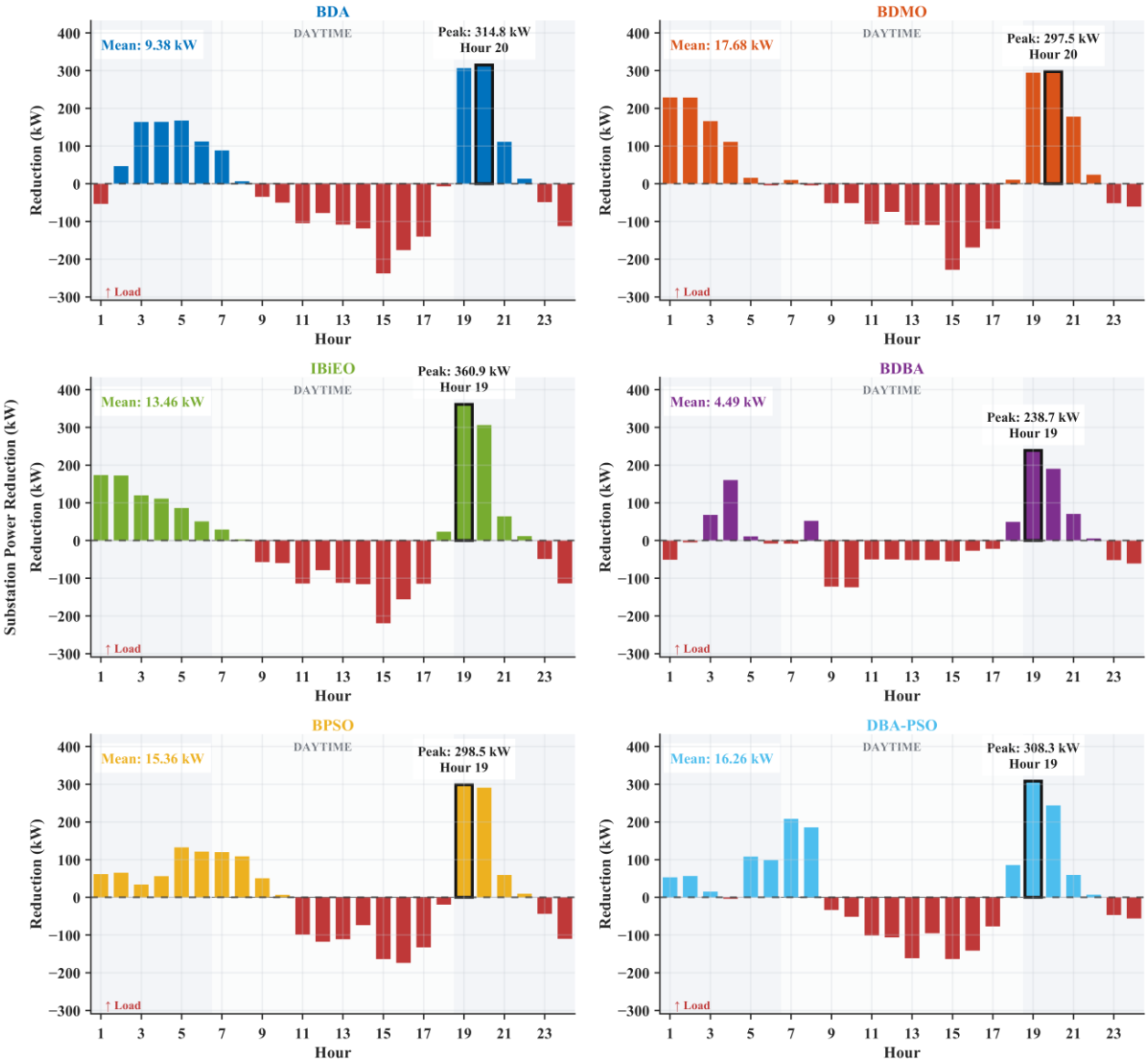


Figure 6. Hourly substation power reduction in the critical scenario for the best run of each algorithm. Positive bars (algorithm color) denote a reduction of the substation power by BESS discharging, and negative (red) bars an increase by charging; the outlined bar marks the largest reduction, and the gray bands mark the hours outside the daytime period (06:00–18:00).

4.3. Duck-Curve Indices

Table 3 reports the improvement of the maximum ramp, peak-to-valley range, evening ramp, and evening peak in the critical scenario and probability-weighted over the ten representative scenarios; Figure 7 shows the latter, which corresponds to the optimized quantity. IBiEO yields the largest probability-weighted improvement: 38.2% in maximum ramp, 47.4% in peak-to-valley range, 53.8% in evening ramp, and 4.9% in evening peak (mean 36.1%). DBA-PSO is close (35.3%, $p = 0.11$), whereas BDMO (28.9%), BDA (28.2%), BPSO (24.9%), and BDBA (8.8%) are significantly inferior (Wilcoxon rank-sum, $p < 10^{-9}$). IBiEO improves every representative scenario, from 7.4% in the low-penetration scenario (10, 0, 10) to 44.0% in (40, 40, 40), whereas BDA, BDMO, BPSO, and BDBA deteriorate scenario (10, 0, 10). In the critical scenario, IBiEO reduces the maximum ramp by 47.6%, the peak-to-valley range by 41.7%, the evening ramp by 52.6%, and the evening peak by 10.4% (mean 38.1%); in this scenario, IBiEO, DBA-PSO (38.6%), BDMO (38.4%), and BDA (37.5%) are statistically indistinguishable ($p \geq 0.47$), whereas BPSO (35.9%, $p = 0.015$) and BDBA (22.2%) are inferior. The ramp reduction of 47.6% approaches the 48.2% share of

the critical buses in the steepest hour (Section 4.1), indicating that the schedules exploit most of the controllable variation. The evening peak decreases by only about 10% because the objective contains no explicit peak term and the six BESSs, sized to the EV demand at their buses, provide 300 kW against a 2.3-MW peak.

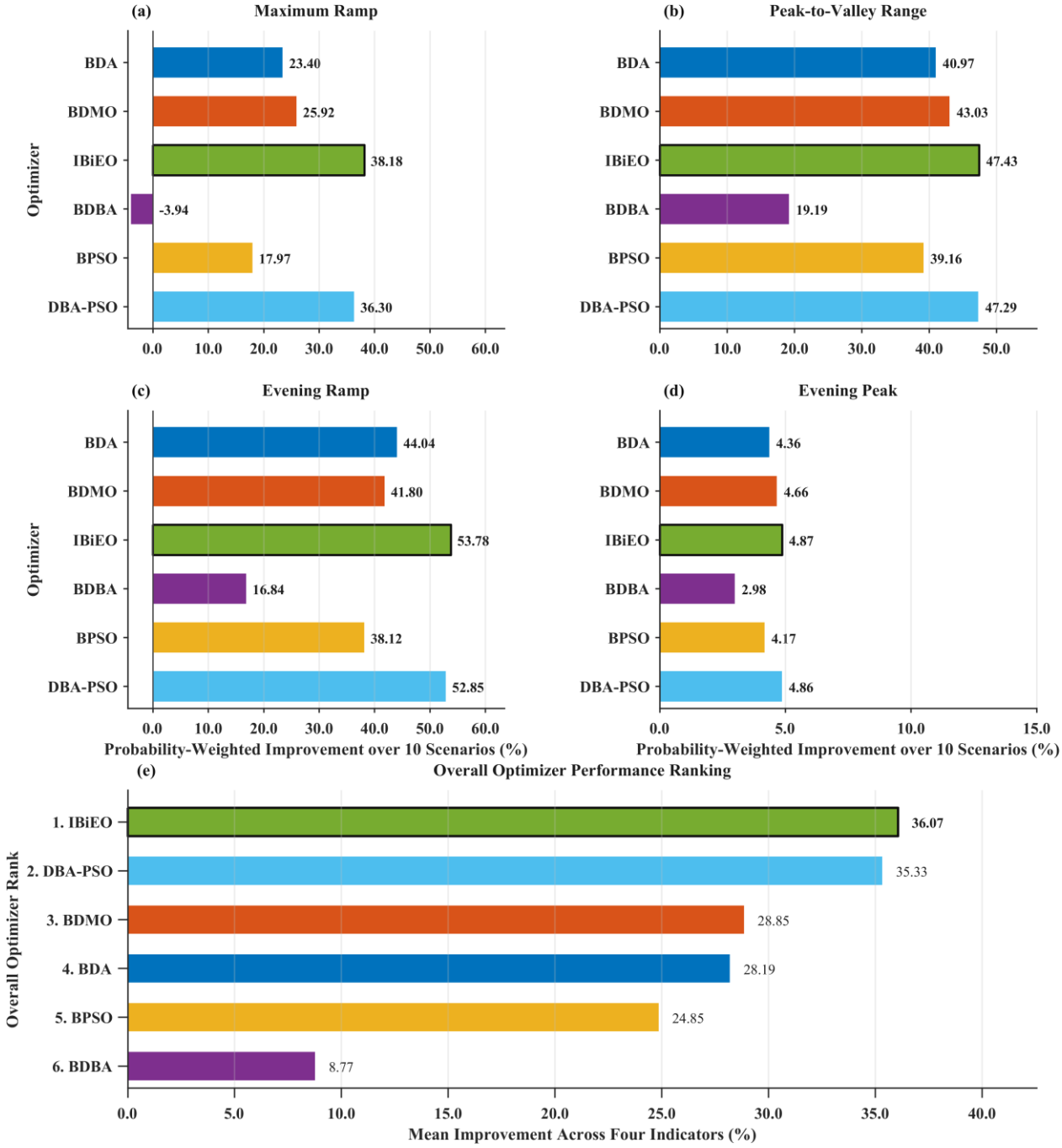


Figure 7. Probability-weighted improvement of the duck-curve indices over 30 runs: (**a**) maximum ramp; (**b**) peak-to-valley range; (**c**) evening ramp; (**d**) evening peak; (**e**) mean of the four indices.

Table 3. Improvement (%) of the duck-curve indices in the critical scenario and probability-weighted over the representative scenarios (mean ± standard deviation over 30 runs).

Algorithm	Max Ramp	Peak–Valley	Evening Ramp	Evening Peak	Mean of Four	Prob.-Weighted Mean of Four
IBiEO	47.6	41.7	52.6	10.4	38.1 ± 3.8	36.1 ± 1.9
DBA-PSO	49.0	41.6	53.4	10.6	38.6 ± 3.5	35.3 ± 1.6
BDMO	48.8	40.2	54.2	10.2	38.4 ± 2.5	28.9 ± 2.4
BDA	49.4	37.8	52.9	10.0	37.5 ± 3.1	28.2 ± 2.1
BPSO	46.4	35.5	51.6	10.0	35.9 ± 2.7	24.9 ± 1.8
BDBA	26.4	21.5	33.9	6.8	22.2 ± 4.3	8.8 ± 2.3

4.4. Overall Performance

Figure 8 shows the convergence and the final expected objective (90). Relative to the no-action reference of 0.0647, IBiEO reduces the mean objective to 0.0412 within 30 iterations and continues to improve until the budget is exhausted, reaching 0.0336. DBA-PSO converges fastest initially (0.0387 after 30 iterations) but stagnates at 0.0341 after about 123 iterations and is overtaken by IBiEO after about 205 iterations; BPSO levels off near 0.041, BDA and BDMO reach 0.0385 and 0.0377 only after a late descent, and BDBA reaches only 0.0529. The final reductions relative to no action are 48.0% for IBiEO, 47.4% for DBA-PSO, 41.8% for BDMO, 40.5% for BDA, 36.9% for BPSO, and 18.3% for BDBA. The sustained improvement of IBiEO is consistent with the memory pool and restart of Section 3.2, which counteract premature stagnation.

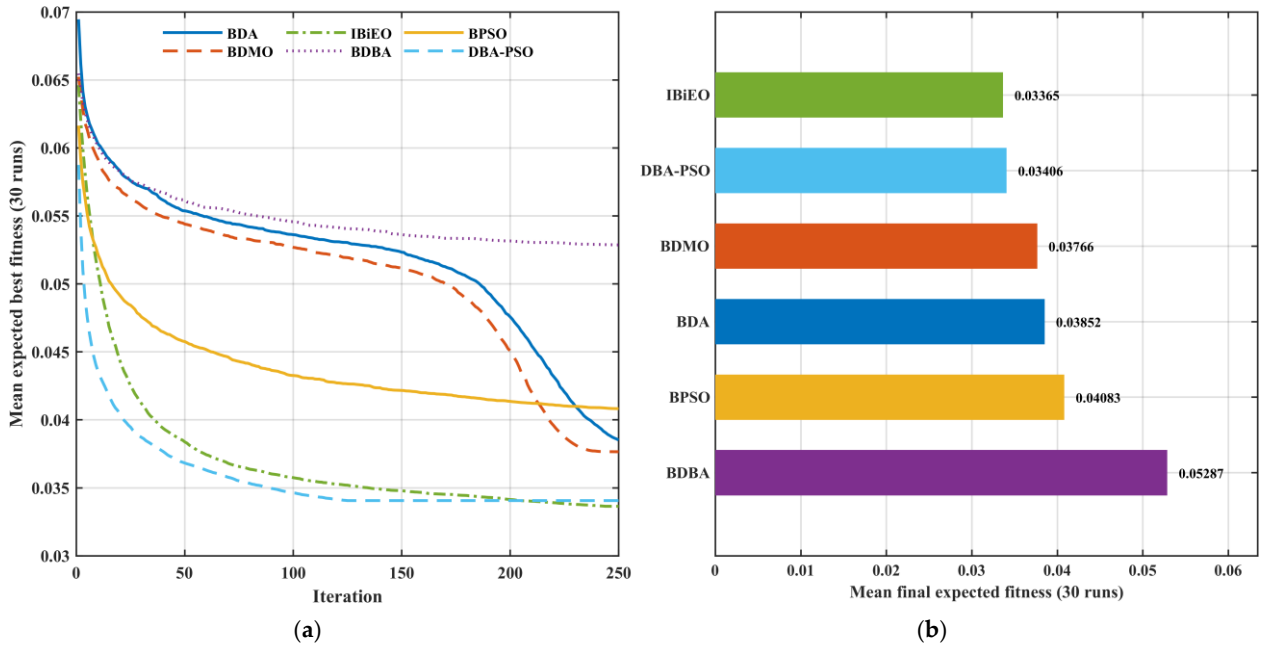


Figure 8. Convergence of the six algorithms over 30 runs: (**a**) mean probability-weighted best objective versus iteration; (**b**) mean final expected objective.

4.5. IBiEO-Based Scheduling of the Critical Buses

Figure 9 shows the IBiEO schedule of the critical scenario (run with the lowest critical-scenario objective) at the six critical buses. All three states occur: 34 of the 144 BESS-hours are discharging, 28 charging, and 82 idle (Figure 9a). Discharging is concentrated in hours 1–7 and at the evening peak, where all six BESSs discharge simultaneously at hours 19–20, while charging occurs from the late morning to hour 18. The net operational index

(Figure 9b) accordingly changes from discharging-dominant at night to charging-dominant at midday and back to full discharge in the evening.

The activity differs between buses (Figure 9c–e): the BESSs at 860 and mid822 operate most (7 discharging and 6 charging hours each), whereas the BESS at mid806 is idle for 16 h, and each unit performs two to three discharge and one to three charge episodes. The schedule is therefore sparse and bus-specific, and the idle hours show that a BESS is activated only when its action reduces the objective.



Figure 9. IBiEO schedule of the critical buses in the critical scenario: (**a**) hourly operating states; (**b**) fraction of charging and discharging BESSs and net operational index; (**c**) daily participation in each state; (**d**) discharge and (**e**) charge activation episodes per bus. In (**a**), the dashed lines and light shading mark the morning transition (hours 8–10) and the evening peak (hours 18–21); in (**b**), the shaded areas indicate the fractions of charging and dis-charging BESSs.

4.6. Statistical Analysis

The statistical significance of the results is assessed on the expected objective (90) of the 30 independent runs of each algorithm, shown as boxplots in Figure 10 and summarized in Table 4. IBiEO has the lowest mean (0.0336) and median (0.0338). The Friedman test, applied to the 30 × 6 matrix of results with one observation per run and algorithm, gives $p = 3.0140\times10^{-29}$, so the null hypothesis of equivalent performance is rejected at $\alpha = 0.05$. The mean Friedman ranks (rank 1 = lowest objective) are 1.37 for IBiEO, 1.63 for DBA-PSO, 3.17 for BDMO, 3.83 for BDA, 5.00 for BPSO, and 6.00 for BDBA.

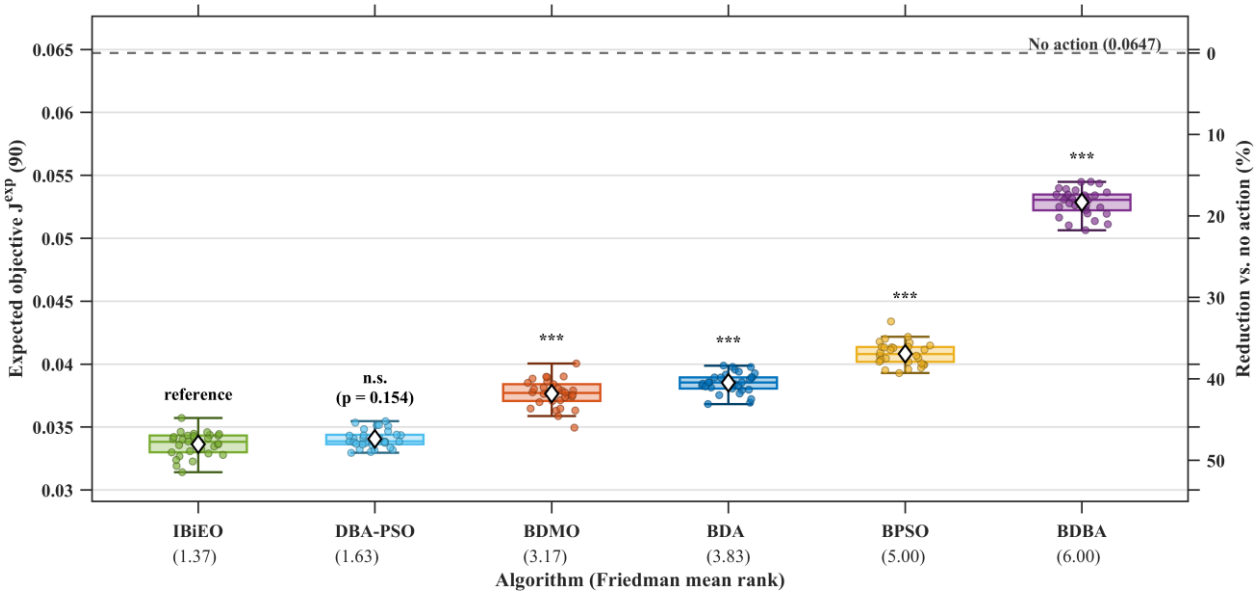


Figure 10. Expected objective (90) of the six algorithms over 30 independent runs. ***, Holm-adjusted $p < 0.001$ versus IBiEO; n.s., not significant; Friedman mean ranks in parentheses.

Pairwise comparisons between IBiEO and each benchmark algorithm use the Wilcoxon rank-sum (Mann–Whitney U) test, because the runs of different algorithms are independent samples; the signed-rank test would require paired observations [48]. To control the family-wise error rate over the five comparisons, the p-values are adjusted with the Holm–Bonferroni procedure [49]. The adjusted p-value is 1.5099×10^{-10} for BDA, BDMO, BPSO, and BDBA, so IBiEO is significantly better than these four algorithms; this is the smallest attainable value for two samples of 30 runs and indicates that every IBiEO run outperformed every run of these algorithms. For DBA-PSO, the adjusted p-value is 0.154; IBiEO has the lower mean and median objective, but the difference is not statistically significant at $\alpha = 0.05$, and the two algorithms are regarded as comparable on this problem. The Kruskal–Wallis test ($p = 1.0287\times10^{-33}$) confirms that the six result distributions are not identical. The one-way ANOVA ($p = 4.1792\times10^{-147}$) leads to the same conclusion; because ANOVA assumes normally distributed residuals with equal variances, which is not guaranteed for metaheuristic results, it is reported only as a supplementary check [48]. In summary, IBiEO ranks first, is significantly better than BDA, BDMO, BPSO, and BDBA, and is statistically comparable to DBA-PSO in objective value, while it gives the largest probability-weighted improvement of the duck-curve indices (Section 4.3).

Table 4. Expected objective (90) and statistical comparison of the six algorithms over 30 independent runs.

Test/statistic	IBiEO	DBA-PSO	BDMO	BDA	BPSO	BDBA
Expected objective: mean	0.03365	0.03406	0.03766	0.03852	0.04083	0.05287
Expected objective: standard deviation	0.00093	0.00071	0.00108	0.00080	0.00091	0.00103
Expected objective: best	0.03142	0.03295	0.03495	0.03683	0.03929	0.05064
Reduction vs. no action (72)	48.0%	47.4%	41.8%	40.5%	36.9%	18.3%
Friedman: mean rank (order)	1.37 (1)	1.63 (2)	3.17 (3)	3.83 (4)	5.00 (5)	6.00 (6)
Friedman: *p*-value	3.0140×10^{-29}					
Rank-sum vs. IBiEO: h-value	–	0	1	1	1	1
Rank-sum vs. IBiEO: *p*-value	–	1.5367×10^{-1}	3.3384×10^{-11}	3.0199×10^{-11}	3.0199×10^{-11}	3.0199×10^{-11}
Rank-sum vs. IBiEO: Holm *p*-value	–	1.5367×10^{-1}	1.5099×10^{-10}	1.5099×10^{-10}	1.5099×10^{-10}	1.5099×10^{-10}
Null hypothesis rejected (α = 0.05)	–	No	Yes	Yes	Yes	Yes
Direction	–	n.s.	IBiEO better	IBiEO better	IBiEO better	IBiEO better
Kruskal–Wallis: *p*-value	1.0287×10^{-33}					
ANOVA: *p*-value	4.1792×10^{-147}					

Rank 1 = lowest objective; h = 1 when the Holm-adjusted rank-sum test rejects equal performance at α = 0.05; n.s. = not significant. No-action reference: 0.06472.

4.7. Propagation of Measurement Uncertainty

The scenarios of Section 2.4 represent the variability of DER penetration, whereas the device parameters within a scenario have so far been treated as exact. In practice, the SOC estimated by battery management systems deviates from the true value; the estimation errors reported for different methods range from below 1% to about 6.5% [50]; the available capacity of lithium-ion batteries decreases markedly at low temperatures [51] and with ageing [41]; and the factory measurement of the PV peak power at standard test conditions has a typical uncertainty of about ±3% [52]. Bounds of ±10% were therefore assumed for the SOC and the usable BESS capacity, deliberately wider than the reported estimation errors, and ±3% for the PV peak power. The effect of these uncertainties on the optimized schedules was evaluated with the Monte Carlo method of JCGM 101:2008 [39] (Figure 11).

Four input quantities were treated as uncertain: the SOC estimate of every EV (±10% of capacity), the SOC estimate of every customer and optimized BESS (±10%), the usable BESS capacity (±10%), and the PV peak power (±3%). As only their limits are known, rectangular distributions were assigned [39], with an independent draw for every device, and the charging time of each EV was recomputed from its true SOC. The schedules were not re-optimized: the six BESSs executed the commands of the run with the median expected objective, and their power followed from (57)–(63) with the true initial SOC and capacity, so that SOC limits could be reached earlier or later than planned.

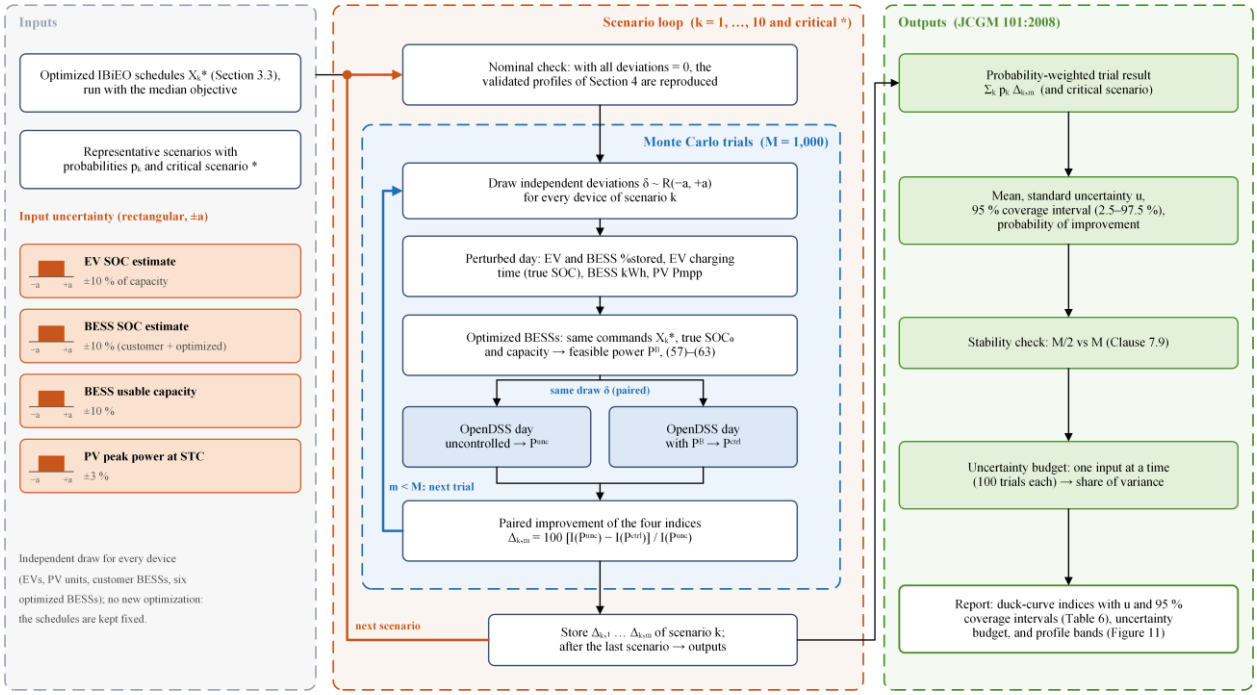


Figure 11. Monte Carlo propagation of measurement uncertainty according to JCGM 101:2008. The asterisk (*) denotes the critical scenario, and $\mathbf{X}_k^*$ the optimized schedule of scenario k.

For each representative scenario and the critical scenario, M = 1000 trials were performed, each consisting of two OpenDSS simulations with the same parameter draw, without and with the optimized BESSs. This pairing isolates the effect of the schedule from the perturbation of the uncontrolled profile. With zero deviations, the procedure reproduces the validated profiles of Section 4 exactly. The probability-weighted trial results yield the mean, the standard uncertainty u, and the probabilistically symmetric 95% coverage interval. Halving M changes the mean by 0.01 and the interval limits by less than 0.3 percentage points, so M = 1000 is adequate (JCGM 101:2008, Clause 7.9). An uncertainty budget was obtained from 100 additional trials per input, with only that input varied. The schedules remain effective under all parameter draws: the mean improvement of the four indices is positive in every trial, both in the critical scenario and probability-weighted (Table 5). Relative to the nominal values of the median run, 41.6% and 33.8%, the improvement decreases to 39.0% (u = 2.6%, 95% interval 33.1–43.6%) in the critical scenario and to 25.2% (u = 2.4%, 20.4–29.7%) probability-weighted. The loss is concentrated in the two ramp indices: because they are maximum values and the schedules are tuned to the nominal profiles, a deviation in any hour can create a new, larger ramp. The peak-to-valley range (41.7%) and the evening peak (4.1%) are nearly unaffected, and the 95% band of the controlled profile stays well below that of the uncontrolled feeder throughout the evening peak (Figure 12).

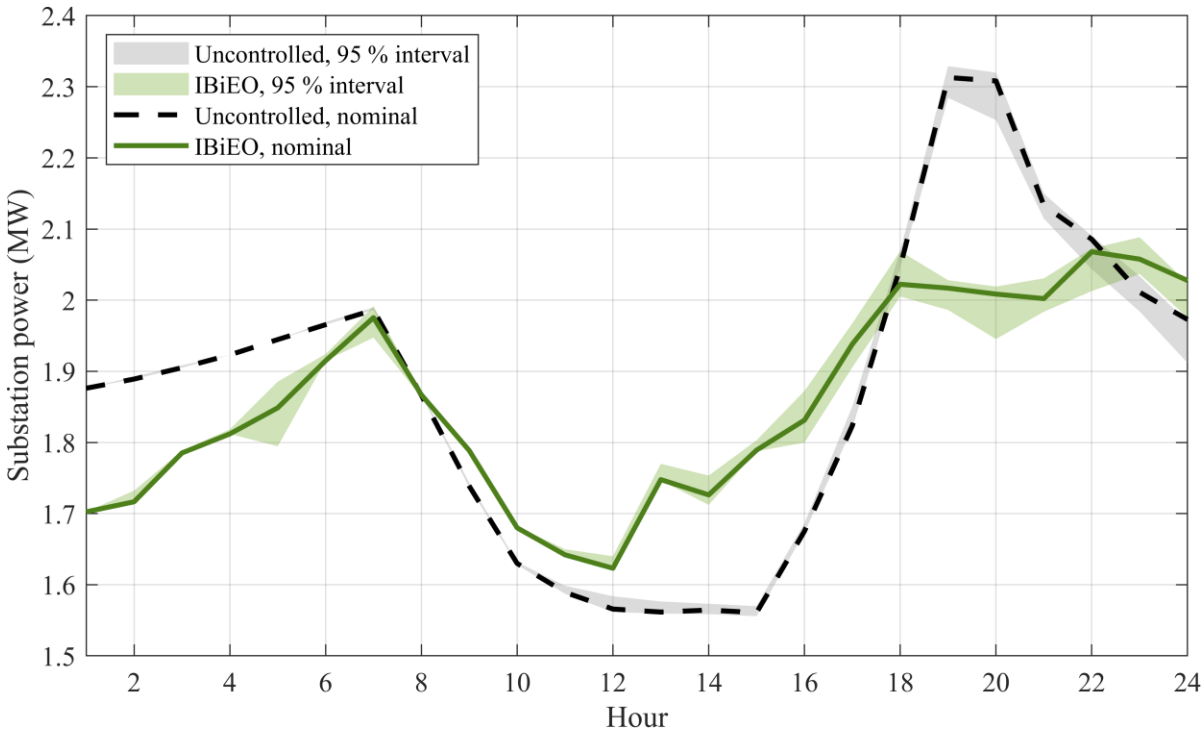


Figure 12. Substation power profiles in the critical scenario under measurement uncertainty: nominal profiles and 95% coverage bands of the uncontrolled feeder and the IBiEO schedule.

The sensitivity varies strongly between scenarios. Scenarios with high PV penetration retain most of their benefit, whereas the low-penetration scenarios are the most fragile: in (10, 0, 10), the schedule of the median run already deteriorates the indices at nominal parameters (−21.2%) and does so in all but 0.1% of the trials (interval −64.4% to −9.9%), while (30, 10, 10) and (0, 10, 30) improve in 93% and 98% of the trials; these scenarios are also the most sensitive to forecast errors (Section 4.8). In the probability-weighted result, the uncertainty budget (Table 5) is dominated by the SOC estimates: the BESS SOC contributes 49% of the variance, the EV SOC 32%, the BESS capacity 18%, and the PV tolerance about 1%. In the critical scenario, which has no customer BESSs, the EV SOC (48%) and the capacity of the six optimized BESSs (47%) contribute almost equally, since the capacity sets the energy available to these units during the evening discharge. Improved SOC estimation and capacity tracking therefore reduce the uncertainty of the benefit far more than tighter PV tolerances, while distributions measured on the feeder are required to replace the assumed limits.

Table 5. Duck-curve improvement (%) under measurement uncertainty of the input parameters (M = 1000 trials per scenario).

Index	Critical: Nominal	Critical: Mean ± u (95% Interval)	Prob.-Weighted: Nominal	Prob.-Weighted: Mean ± u (95% Interval)
Maximum ramp	53.2	47.3 ± 3.9 (39.1–53.8)	35.6	23.0 ± 4.5 (13.6–31.2)
Peak-to-valley range	40.9	41.7 ± 1.8 (38.0–45.3)	43.2	41.7 ± 1.5 (38.8–44.6)
Evening ramp	59.8	55.2 ± 6.8 (40.4–67.6)	51.9	31.9 ± 5.4 (21.2–42.1)
Evening peak	12.6	11.8 ± 0.7 (10.3–12.9)	4.5	4.1 ± 0.3 (3.6–4.6)
Mean of the four indices	41.6	39.0 ± 2.6 (33.1–43.6)	33.8	25.2 ± 2.4 (20.4–29.7)
Uncertainty budget of the four-index mean: u (share of variance)				
EV SOC, ±10%		2.1 (48%)		1.3 (32%)
BESS SOC, ±10%		0.7 (5%)		1.6 (49%)
BESS capacity, ±10%		2.1 (47%)		1.0 (18%)
PV peak power, ±3%		0.3 (1%)		0.3 (1%)

4.8. Robustness: Forecast Error and BESS Size

Two analyses assess the robustness of the scenario-specific schedules (Table 6). First, forecast errors were emulated by applying the IBiEO schedule of each scenario to every other scenario in OpenDSS. Selecting the nearest wrong scenario in the (EV, PV, BESS) space reduces the probability-weighted improvement from 36.1% to 13.3%, whereas a random wrong scenario yields −12.3%; the low-penetration scenarios (10, 0, 10), (30, 10, 10), and (0, 10, 30) are the most sensitive, so forecast accuracy on low-PV days governs the practical benefit. Second, doubling the BESS rating to 100 kW/400 kWh improves the critical scenario (maximum ramp −51.2%, peak-to-valley range −56.5%, evening ramp −63.6%, evening peak −13.8%) but lowers the probability-weighted improvement to 15.3% and the objective reduction from 48.0% to 38.8%, because a 100-kW step exceeds the 50–60-kW ramps of the low-penetration scenarios. Under all-or-nothing switching, the 50-kW rating matched to the EV demand at the critical buses is therefore preferable; larger units require several power levels per block.

Table 6. Robustness of the IBiEO schedules to forecast errors and BESS size (mean over 30 runs).

Case	Critical Scenario	Probability-Weighted	Objective Reduction vs. No Action
Scenario-specific schedules, 50 kW/200 kWh (main case)	38.1	36.1	48.0%
Scenario-specific, nearest wrong scenario forecast	–	13.3	–
Scenario-specific, random wrong scenario forecast	–	−12.3	–
Scenario-specific schedules, 100 kW/400 kWh	46.3	15.3	38.8%

5. Conclusions

This paper presented a probabilistic BESS scheduling framework for mitigating the duck curve in distribution systems with uncertain and correlated DER penetration, combining dependence-aware scenario generation, fuzzy weighting and reduction, OpenDSS baselines, variability-based BESS location, and scenario-specific three-state schedules optimized with an improved binary Equilibrium Optimizer. Under identical budgets and seeds on the IEEE 34-bus feeder, IBiEO achieved the lowest expected objective (0.0336, 48.0% below no action) and the best Friedman rank (1.37); it was significantly better than BDA, BDMO, BPSO, and BDBA and statistically comparable to DBA-PSO. Its OpenDSS-validated schedules improved the probability-weighted duck-curve indices by 36.1% (maximum ramp 38.2%, peak-to-valley range 47.4%, evening ramp 53.8%), improved every representative scenario, and reduced the maximum ramp of the critical scenario by 47.6%, close to the 48.2% share of the critical buses in the steepest hour. Under the measurement uncertainty of SOC, BESS capacity, and PV peak power, propagated according to JCGM 101:2008, the probability-weighted improvement remained 25.2% (95% interval 20.4–29.7%) and was positive in every trial, with the SOC estimates as the dominant source of uncertainty. Three findings extend beyond this case study: the BESSs must be able to remain idle; the benefit of scenario-specific schedules selected by a day-ahead forecast depends on forecast accuracy, because errors on low-PV days erode it; and under all-or-nothing switching, the BESS power step should not exceed the ramps it is meant to correct. The limited evening-peak reduction (about 10%) reflects the absence of an explicit peak term and the 300-kW BESS rating against a 2.3-MW peak. Future work will address larger feeders, multi-level BESS power and sizing, rolling or recourse scheduling robust to forecast errors, BESS degradation, and measured parameter distributions.

Author Contributions: Conceptualization, S.M.A.; Methodology, S.M.A.; Software, S.M.A.; Validation, S.M.A. and Y.O.A.; Formal analysis, S.M.A.; Investigation, S.M.A.; Resources, S.M.A. and A.F.; Data curation, S.M.A.; Writing—original draft, S.M.A.; Writing—review & editing, S.M.A. and A.F.; Visualization, S.M.A. All authors have read and agreed to the published version of the manuscript.

Funding: This work was funded by the Deanship of Graduate Studies and Scientific Research at Jouf University under grant No. (DGSSR-2026-02-01336).

Data Availability Statement: The original contributions presented in this study are included in the article. Further inquiries can be directed to the corresponding author.

Acknowledgments: During the preparation of this manuscript, the authors used ChatGPT (GPT-6; OpenAI, San Francisco, CA, USA, 2026) for the purposes of language editing during the preparation of the manuscript. It was used to check grammar, improve sentence clarity, and review the flow and readability of the text. ChatGPT was not used for the research, methodology, simulations, data analysis, or generation of results and conclusions. The authors have reviewed and edited the output and take full responsibility for the content of this publication.

Conflicts of Interest: The authors declare no conflict of interest.

References

1. Al-Shetwi, A.Q.; Hannan, M.A.; Jern, K.P.; Mansur, M.; Mahlia, T.M.I. Grid-Connected Renewable Energy Sources: Review of the Recent Integration Require. *J. Clean. Prod.* **2020**, *253*, 119831.
2. Obi, M.; Bass, R. Trends and Challenges of Grid-Connected Photovoltaic Systems–A Review. *Renew. Sustain. Energy Rev.* **2016**, *58*, 1082–1094.
3. St John, J. *The California Duck Curve Is Real, and Bigger than Expected*; Green Tech Media: Boston, MA, USA, 2016.
4. Krietemeyer, B.; Dedrick, J.; Sabaghian, E.; Rakha, T. Managing the Duck Curve: Energy Culture and Participation in Local Energy Management Programs in the United States. *Energy Res. Soc. Sci.* **2021**, *79*, 102055.
5. Gupta, R.S.; Tyagi, A.; Anand, S. Optimal Allocation of Electric Vehicles Charging Infrastructure, Policies and Future Trends. *J. Energy Storage* **2021**, *43*, 103291.
6. Singh, B.; Sharma, A.K. Benefit Maximization and Optimal Scheduling of Renewable Energy Sources Integrated System Considering the Impact of Energy Storage Device and Plug-in Electric Vehicle Load Demand. *J. Energy Storage* **2022**, *54*, 105245.
7. Jovanovic, R.; Bayhan, S.; Bayram, I.S. A Multiobjective Analysis of the Potential of Scheduling Electrical Vehicle Charging for Flattening the Duck Curve. *J. Comput. Sci.* **2021**, *48*, 101262.
8. Palmiotto, F.; Zhou, Y.; Forte, G.; Dicorato, M.; Trovato, M.; Cipcigan, L.M. A Coordinated Optimal Programming Scheme for an Electric Vehicle Fleet in the Residential Sector. *Sustain. Energy Grids Netw.* **2021**, *28*, 100550.
9. He, Z.; Khazaei, J.; Freihaut, J.D. Optimal Integration of Vehicle to Building (V2B) and Building to Vehicle (B2V) Technologies for Commercial Buildings. *Sustain. Energy Grids Netw.* **2022**, *32*, 100921.
10. Fachrizal, R.; Shepero, M.; van der Meer, D.; Munkhammar, J.; Widén, J. Smart Charging of Electric Vehicles Considering Photovoltaic Power Production and Electricity Consumption: A Review. *ETransportation* **2020**, *4*, 100056.
11. Kalair, A.R.; Abas, N.; Seyedmahmoudian, M.; Rauf, S.; Stojcevski, A.; Khan, N. Duck Curve Leveling in Renewable Energy Integrated Grids Using Internet of Relays. *J. Clean. Prod.* **2021**, *294*, 126294.
12. Calero, I.; Canizares, C.A.; Bhattacharya, K.; Baldick, R. Duck-Curve Mitigation in Power Grids with High Penetration of PV Generation. *IEEE Trans. Smart Grid* **2021**, *13*, 314–329.
13. Reddivari, R.; Jena, D. Improved Gamma Type Y-Source Inverter for Rooftop PV Based VG Applications. *Int. J. Electr. Power Energy Syst.* **2022**, *142*, 108261.
14. Shigenobu, R.; Ito, M.; Taoka, H. Optimal Design of Bifacial PV System to Mitigate Duck-Curve Problem of Power System with the UC Problem. *Energy Rep.* **2021**, *7*, 7004–7014.
15. Ahmad, S.S.; Al-Ismail, F.S.; Almehizia, A.A.; Khalid, M. Model Predictive Control Approach for Optimal Power Dispatch and Duck Curve Handling under High Photovoltaic Power Penetration. *IEEE Access* **2020**, *8*, 186840–186850.
16. Rouholamini, M.; Chen, L.; Wang, C. Modeling, Configuration, and Grid Integration Analysis of Bifacial PV Arrays. *IEEE Trans. Sustain. Energy* **2020**, *12*, 1242–1255.

17. Singh, D.K.; Maurya, S.K.; Goyal, S. *Duck Curve Characterization, Challenges and Mitigation Techniques: An Extensive Analysis*; IEEE: New York, NY, USA, 2026; pp. 239–243.
18. Sheha, M.; Mohammadi, K.; Powell, K. Solving the Duck Curve in a Smart Grid Environment Using a Non-Cooperative Game Theory and Dynamic Pricing Profiles. *Energy Convers. Manag.* **2020**, *220*, 113102.
19. Zargari, N.; Ofir, R.; Chowdhury, N.R.; Belikov, J.; Levron, Y. An Optimal Control Method for Storage Systems with Ramp Constraints, Based on an On-Going Trimming Process. *IEEE Trans. Control Syst. Technol.* **2022**, *31*, 493–496.
20. Su, H.Y.; Liu, J.H.; Chu, C.C.; Lee, S.H.; Hong, Y.Y.; Lin, Y.J.; Liao, C.J. Developing an Optimal Scheduling of Taiwan Power System with Highly Penetrated Renewable Energy Resources and Pumped Hydro Storages. *IEEE Trans. Ind. Appl.* **2021**, *57*, 314–329.
21. Kim, H.; Heo, S.; Park, J. Economic Mitigation Strategy for the Duck Curve Phenomenon: Revealing the Effectiveness of Green Hydrogen. *Energy* **2026**, *362*, 142158.
22. Paul, W.U.H.; Siddiqui, A.S.; Kirmani, S. An Effective Duck Curve Problem Solution Using Intelligent Hybrid Optimization. *J. Eng. Sci. Technol. Rev.* **2026**, *19*, 76.
23. Behbahani, F.M.; Ceylan, O.; Ozdemir, A. *Optimum Scheduling of Energy Storage Systems in Distribution Grids to Minimize the Duck Curve Slope*; IEEE: New York, NY, USA, 2025; pp. 1–6.
24. Nyangon, J. Smart Grid Strategies for Tackling the Duck Curve: A Qualitative Assessment of Digitalization, Battery Energy Storage, and Managed Rebound Effects Benefits. *Energies* **2025**, *18*, 3988.
25. Olczak, P. Maximum Charging and Discharging Power for Households Electrical Battery Cooperated with PV. *J. Energy Storage* **2026**, *150*, 120364.
26. Tsushima, Y.; Shigeyasu, T. *An Efficient Battery Migration Strategy for Duck Curve Alleviation in Battery Swapping EV Infrastructure*; Springer Nature: Cham, Switzerland, 2025; pp. 232–243.
27. Georgiou, G.S.; Nikolaidis, P.; Christodoulides, P. Distributed Battery Energy Storage in Modern Power Systems: Artificial-Intelligence-Driven Optimization for Utility-Substation Autonomy Expansion and Residual Load Flattening. *J. Energy Storage* **2026**, *176*, 123317.
28. Hou, Q.; Zhang, N.; Du, E.; Miao, M.; Peng, F.; Kang, C. Probabilistic Duck Curve in High PV Penetration Power System: Concept, Modeling, and Empirical Analysis in China. *Appl. Energy* **2019**, *242*, 205–215.
29. Forbes, K.F. Demand for Grid-Supplied Electricity in the Presence of Distributed Solar Energy Resources: Evidence from New York City. *Util. Policy* **2023**, *80*, 101447.
30. Kwon, O.; Lee, S.; Park, J. A Numerical Study to Compensate Duck Curve of ESS Integrated Gas Turbine System with Reused-Battery. *J. Energy Storage* **2022**, *55*, 105422.
31. Gomes, I.S.F.; Perez, Y.; Suomalainen, E. Rate Design with Distributed Energy Resources and Electric Vehicles: A Californian Case Study. *Energy Econ.* **2021**, *102*, 105501.
32. Esfahani, S.K.; Tenorio, R.; Karrech, A.; Defendi, K.; Jerez, F. Analysing the Role of Roof Mounted BIPV System Optimization on Decreasing the Effect of Duck Curve in Perth, Western Australia: An Experimental Case Study. *Sustain. Energy Technol. Assess.* **2021**, *47*, 101328.
33. Wong, L.A.; Ramachandaramurthy, V.K.; Walker, S.L.; Ekanayake, J.B. Optimal Placement and Sizing of Battery Energy Storage System Considering the Duck Curve Phenomenon. *IEEE Access* **2020**, *8*, 197236–197248.
34. Chakraborty, S.; Modi, G.; Singh, B.; Panigrahi, B.K.; Das, S.; Roy, S. Peak Shaving and Duck Curve Mitigation with BES Based Ramp Rate Limit Strategy for Power Quality Enhancement of SPV-BES Microgrid. *IEEE Trans. Ind. Appl.* **2024**, *61*, 1234–1245.
35. Chen, Y.; Liu, J.; Yu, D. Wind Meets Solar: Crafting the Perfect Duck Curve for Future Power Systems. *J. Atmos. Sol.-Terr. Phys.* **2025**, *277*, 106664.
36. Zahedi, R.; Gadh, R. *Mitigating the Duck Curve and Grid Upgrade in Design of Heavy-Duty Electric Vehicle Charging Infrastructure*; IEEE: New York, NY, USA, 2026; pp. 1–5.
37. Reddy, K.H.; Pushparaj, H.; Reddy, G.B.; Sekhar, S.C.; Mahesh, G.S.; Babu, G.D. *Optimized Machine Learning-Based Multi-Pumped Storage Scheduling for Renewable Grids Using Synthetic Data and Duck Curve Mitigation*; IEEE: New York, NY, USA, 2025; pp. 1–7.
38. Durán-Castillo, G.; Weis, T.; Leach, A.; Fleck, B.A. Toward Sustainable Electricity Markets: Merit-Order Dynamics on Photovoltaic Energy Price Duck Curve and Emissions Displacement. *Sustainability* **2025**, *17*, 4618.
39. Joint Committee for Guides in Metrology. *Evaluation of Measurement Data—Supplement 1 to the "Guide to the Expression of Uncertainty in Measurement"—Propagation of Distributions Using a Monte Carlo Method*; Joint Committee for Guides in Metrology: Sèvres, France, 2008.

40. Tesla, Inc. Powerwall 2 AC Datasheet (North America). Available online: https://www.tesla.com/sites/default/files/pdfs/powerwall/Powerwall%202_AC_Datasheet_en_northamerica.pdf (accessed on 10 September 2026).
41. Hesse, H.C.; Schimpe, M.; Kucevic, D.; Jossen, A. Lithium-Ion Battery Storage for the Grid—A Review of Stationary Battery Storage System Design Tailored for Applications in Modern Power Grids. *Energies* **2017**, *10*, 2107.
42. Badole, S.B.; Firestone, J.; Heintzelman, M.D.; Parsons, G. Co-Adoption of Solar Panels and Electric Vehicles: Evidence from California. *Transp. Res. Part D Transp. Environ.* **2026**, *158*, 105450.
43. Shen, X.; Qiu, Y.L.; Bo, X.; Patwardhan, A.; Hultman, N.; Dong, B. The Impact of Co-Adopting Electric Vehicles, Solar Photovoltaics, and Battery Storage on Electricity Consumption Patterns: Empirical Evidence from Arizona. *Resour. Conserv. Recycl.* **2023**, *192*, 106914.
44. Faramarzi, A.; Heidarinejad, M.; Stephens, B.; Mirjalili, S. Equilibrium Optimizer: A Novel Optimization Algorithm. *Knowl.-Based Syst.* **2020**, *191*, 105190.
45. Faramarzi, A.; Mirjalili, S.; Heidarinejad, M. Binary Equilibrium Optimizer: Theory and Application in Building Optimal Control Problems. *Energy Build.* **2022**, *277*, 112503.
46. Wolpert, D.H.; Macready, W.G. No Free Lunch Theorems for Optimization. *IEEE Trans. Evol. Comput.* **1997**, *1*, 67–82.
47. Mirjalili, S.; Lewis, A. S-Shaped versus V-Shaped Transfer Functions for Binary Particle Swarm Optimization. *Swarm Evol. Comput.* **2013**, *9*, 1–14.
48. Derrac, J.; García, S.; Molina, D.; Herrera, F. A Practical Tutorial on the Use of Nonparametric Statistical Tests as a Methodology for Comparing Evolutionary and Swarm Intelligence Algorithms. *Swarm Evol. Comput.* **2011**, *1*, 3–18.
49. Holm, S. A Simple Sequentially Rejective Multiple Test Procedure. *Scand. J. Stat.* **1979**, *6*, 65–70.
50. Hannan, M.A.; Lipu, M.S.H.; Hussain, A.; Mohamed, A. A Review of Lithium-Ion Battery State of Charge Estimation and Management System in Electric Vehicle Applications: Challenges and Recommendations. *Renew. Sustain. Energy Rev.* **2017**, *78*, 834–854.
51. Ma, S.; Jiang, M.; Tao, P.; Song, C.; Wu, J.; Wang, J.; Deng, T.; Shang, W. Temperature Effect and Thermal Impact in Lithium-Ion Batteries: A Review. *Prog. Nat. Sci. Mater. Int.* **2018**, *28*, 653–666.
52. Pavanello, D.; Sample, T.; Müllejans, H. An Investigation on the Uncertainty of Fill Factor. *EPJ Photovolt.* **2025**, *16*, 2.

Disclaimer/Publisher's Note: The statements, opinions and data contained in all publications are solely those of the individual author(s) and contributor(s) and not of MDPI and/or the editor(s). MDPI and/or the editor(s) disclaim responsibility for any injury to people or property resulting from any ideas, methods, instructions or products referred to in the content.